

Abstract

Measurement of total hadronic differential cross sections in the LArIAT experiment

Elena Gramellini

2018

6 Abstract goes here. Limit 750 words.

Measurement of total hadronic differential cross sections in the LArIAT experiment

A Dissertation
Presented to the Faculty of the Graduate School
of
Yale University
in Candidacy for the Degree of
Doctor of Philosophy

15 by
16 Elena Gramellini

¹⁷ Dissertation Director: Bonnie T. Fleming

18 Date you'll receive your degree

¹⁹

Copyright © 2017 by Elena Gramellini

²⁰

All rights reserved.

²¹ Contents

²² Acknowledgements	^{iv}
²³ 0 LArIAT: Liquid Argon In A Testbeam	¹
²⁴ 0.1 The Particles' Path to LArIAT	¹
²⁵ 0.2 LArIAT Tertiary Beam Instrumentation	⁴
²⁶ 0.2.1 Bending Magnets	⁴
²⁷ 0.2.2 Multi-Wire Proportional Chambers	⁶
²⁸ 0.2.3 Time-of-Flight System	⁸
²⁹ 0.2.4 Punch-Through and Muon Range Stack Instruments	⁹
³⁰ 0.2.5 LArIAT Cosmic Ray Paddle Detectors	¹¹
³¹ 0.3 In the Cryostat	¹²
³² 0.3.1 Cryogenics and Argon Purity	¹²
³³ 0.3.2 LArTPC: Charge Collection	¹⁵
³⁴ 0.3.3 LArTPC: Light Collection System	¹⁹
³⁵ 0.4 Trigger and DAQ	²⁰
³⁶ 0.5 Control Systems	²²
³⁷ A Measurement of LArIAT Electric Field	²⁷

³⁸ Acknowledgements

³⁹ A lot of people are awesome, especially you, since you probably agreed to read this
⁴⁰ when it was a draft.

⁴¹ **Chapter 0**

⁴² **LArIAT: Liquid Argon In A**

⁴³ **Testbeam**

⁴⁴ In this chapter, we describe the LArIAT experimental setup. We start by illustrating
⁴⁵ the journey of the charged particles in the Fermilab accelerator complex, from
⁴⁶ the gaseous thermal hydrogen at the Fermilab ion source to the delivery of the LAr-
⁴⁷ IAT tertiary beam at MC7. We then describe the LArIAT beamline detectors, the
⁴⁸ LArTPC, the DAQ and the monitoring system.

⁴⁹ **0.1 The Particles' Path to LArIAT**

⁵⁰ LArIAT's particle history begins in the Fermilab accelerator complex with a beam of
⁵¹ protons. The process of proton acceleration develops in gradual stages (see picture
⁵² 1): gaseous hydrogen is ionized in order to form H^- ions; these ions are boosted to
⁵³ 750 keV by a Cockcroft-Walton accelerator and injected into the linear accelerator
⁵⁴ (Linac) that increases their energy up to 400 MeV; then, H^- ions pass through a
⁵⁵ carbon foil and lose the two electrons; the resulting protons are then injected into a
⁵⁶ rapid cycling synchrotron, called the Booster; at this stage, protons reach 8 GeV of
⁵⁷ energy and are compacted into bunches; the next stage of acceleration is the Main

58 Injector, a synchrotron which accelerates the bunches up to 120 GeV; in the Main
59 Injector, several bunches are merged into one and are ready for delivery.

60 The Fermilab accelerator complex works in supercycles of 60 seconds in duration.

61 A 120 GeV primary proton beam with variable intensity is extracted in four-second
62 “spills” and sent to the Meson Center beam line.

63 LArIAT’s home at Fermilab is the Fermilab Test Beam Facility (FTBF), where
64 the experiment characterizes a beam of charged particles in the Meson Center beam
65 line. At FTBF, the primary beam is focused onto a tungsten target to create LAr-
66 IAT’s secondary beam. The secondary beamline is set such that the composition of
67 the secondary particle beam is mainly positive pions. The momentum peak of the
68 secondary beam was fixed at 64 GeV/c for the LArIAT data considered in this work,
69 although the beam is tunable in momentum between 8-80 GeV/c; this configuration
70 of the secondary beamline assured a stable beam delivery at the LArIAT experimental
71 hall.

72 The secondary beam impinges then on a copper target within a steel collimator
73 inside the LArIAT experimental hall (MC7) to create the LArIAT tertiary beam,
74 (shown in Fig. 2). The steel collimator selects particles produced with a 13° pro-
75 duction angle. The particles are then bent by roughly 10° through a pair of dipole
76 magnets. By configuring the field intensity of the magnets we allow the particles of
77 LArIAT’s tertiary beam to span a momentum range from 0.2 to 1.4 GeV/c. The
78 polarity of the magnet is also configurable and determines the sign of the beamline
79 particles which are focused on the LArTPC. If the magnet polarity is positive the
80 tertiary beam composition is mostly pions and protons with a small fraction of elec-
81 trons, muons, and kaons. It is the job of the LArIAT beamline equipment to select the
82 particles polarity, to perform particle identification in the beamline and to measure
83 the momentum of the tertiary beam particles before they get to the LArTPC. The
84 LArIAT detectors are described in the following paragraphs.

Fermilab Accelerator Complex

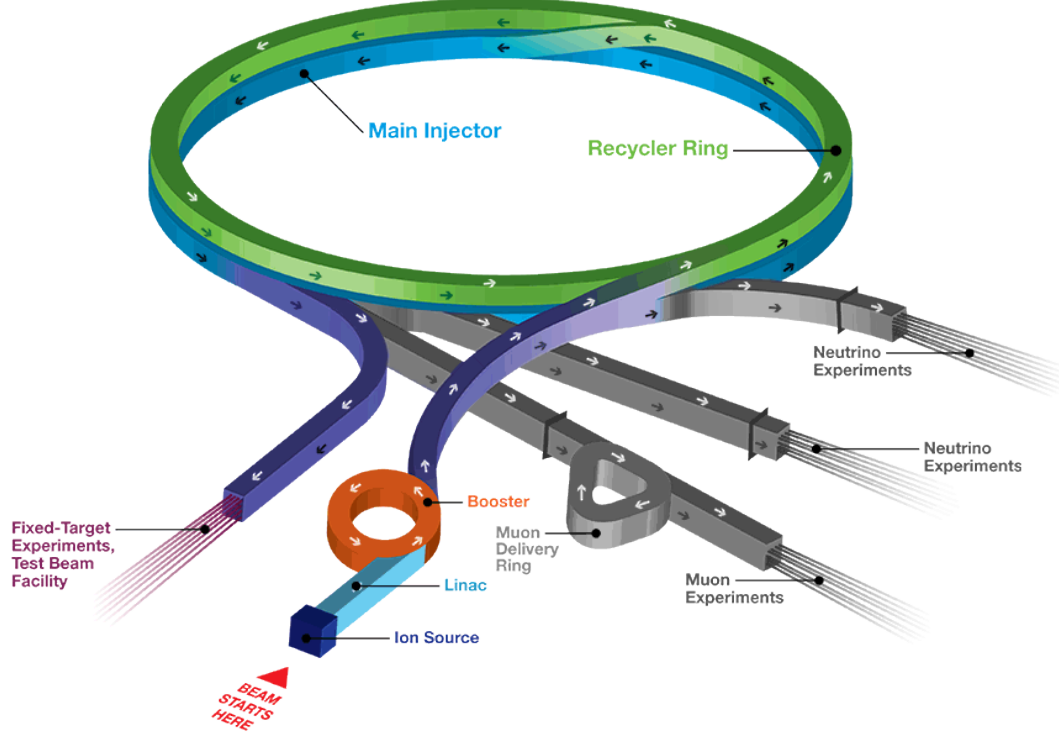


Figure 1: Layout of Fermilab Accelerator complex.

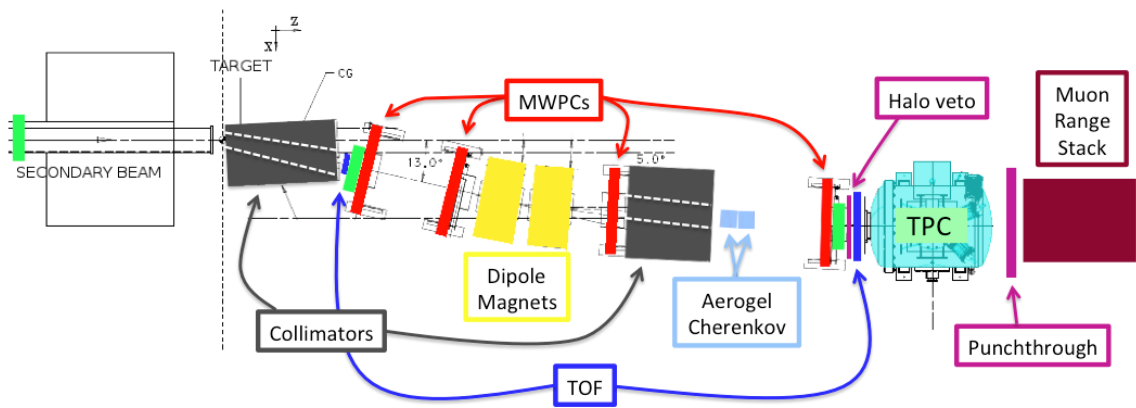


Figure 2: Bird's eye view of the LArIAT tertiary beamline. In grey: upstream and downstream collimators; in yellow: bending magnets; in red: multi wire proportional chambers; in blue: time of flight; in green: liquid argon TPC volume; in maroon: muon range stack.

85 0.2 LArIAT Tertiary Beam Instrumentation

86 The instrumentation of LArIAT tertiary beam and the TPC components have changed
87 several times during the three years of LArIAT data taking. The following paragraphs
88 describe the components operational during “Run II”, the data taking period relevant
89 to the hadron cross section measurements considered in this thesis.

90 The key components of the tertiary beamline instrumentation for the hadron cross
91 section analyses are the two bending magnets, a set of four wire chambers (WCs)
92 and two time-of-flight scintillating paddles (TOF) and, of course, the LArTPC. The
93 magnets determine the polarity of the particles in the tertiary beam; the combination
94 of magnets and wire chambers determines the particles’ momenta, which is used to
95 determine the particle species in conjunction with the TOF. A muon range stack
96 downstream from the TPC and two sets of cosmic paddles configured as a telescope
97 surrounding the TPC are also used for calibration purposes.

98 0.2.1 Bending Magnets

99 LArIAT uses a pair of identical Fermilab type “NDB” electromagnets, recycled from
100 the Tevatron’s anti-proton ring, in a similar configuration used for the MINERvA T-
101 977 test beam calibration [51]. The magnets are a fundamental piece of the LArIAT
102 beamline equipment, as they are used for the selection of the particle polarity and
103 for the momentum measurement before the LArTPC. The sign of the current in the
104 magnets allows us to select either positively or negatively charged particles; the value
105 of the magnetic field is used in the momentum determination and in the subsequent
106 particle identification.

107 We describe here the characteristics and response of one magnet, as the second one
108 has a similar response, given its identical shape and history. Each magnet is a box with
109 a rectangular aperture gap in the center to allow for the particle passage. The magnet

110 aperture measures 14.22 cm in height, 31.75 cm in width, and 46.67 cm in length.
 111 Since the wire chambers aperture (~ 12.8 cm 2) is smaller than the magnet aperture,
 112 only the central part of the magnet gap is utilized. The field is extremely uniform
 113 over this limited aperture and was measured with two hall probes, both calibrated
 114 with nuclear magnetic resonance probes. The probes measured the excitation curve
 115 shown in Figure 3.

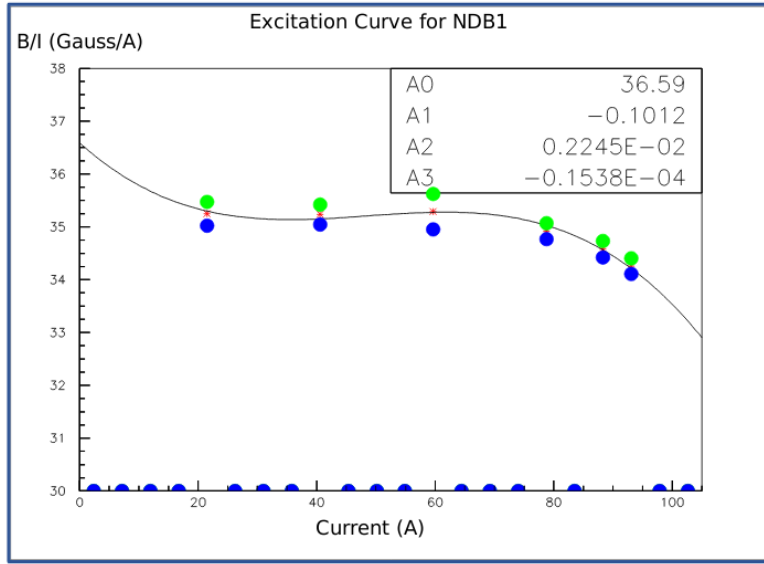


Figure 3: Magnetic field over current as a function of the current, for one NDB magnet (excitation curve). The data was collected using two hall probes (blue and green). We fit the readings with a cubic function (black) to average of measurements (red) given in the legend [38].

116 The current through the magnets at a given time is identical in both magnets.
 117 For the Run II data taking period, the current settings explored were 60A ($B \sim 0.21$
 118 T) and 100A ($B \sim 0.35$ T) in both polarities. Albeit advantageous to enrich the
 119 tertiary beam composition with high mass particles such as kaons, we never pushed
 120 the magnets current over 100 A, not to incur in overheating. During operation, we
 121 operated an air and water cooling system on the magnets and we remotely monitored
 122 the magnet temperatures.

₁₂₃ **0.2.2 Multi-Wire Proportional Chambers**

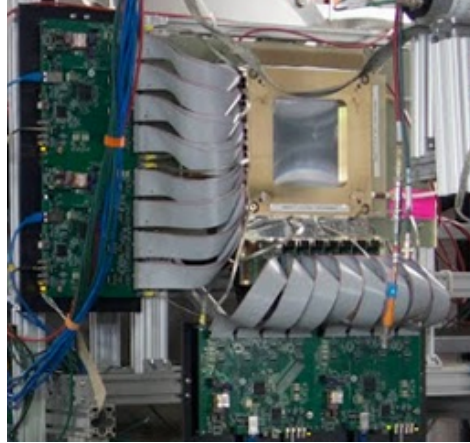


Figure 4: One of the four Multi Wire Proportional Chambers (WC) used in the LArIAT tertiary beamline and related read-out electronics.

₁₂₄ LArIAT uses four multi-wire proportional chambers, or wire chambers (WC) for
₁₂₅ short, two upstream and two downstream from the bending magnets. The geometry
₁₂₆ of one chamber is shown in Figure 4: the WC effective aperture is a square of 12.8 cm
₁₂₇ perpendicular to the beam direction. Inside the chamber, the 128 horizontal and 128
₁₂₈ vertical wires strung at a distance of 1 mm from each other in a mixture of 85% Argon
₁₂₉ and 15% isobutane gas. The WC operating voltage is between 2400 V and 2500 V.
₁₃₀ The LArIAT wire chambers are an upgraded version of the Fenker Chambers [57],
₁₃₁ where an extra grounding improves the signal to noise ratio of the electronic readout.

₁₃₂ Two ASDQ chips [89] mounted on a mother board plugged into the chamber serve
₁₃₃ as front end amplifier/discriminator. The chips are connected to a multi-hit TDC [68]
₁₃₄ which provides a fast OR output used as first level trigger. The TDC time resolution
₁₃₅ is 1.18 ns/bin and can accept 2 edges per 9 ns. The maximum event rate acceptable
₁₃₆ by the chamber system is 1 MHz: this rate is not a limiting factor considering that
₁₃₇ the rate of the tertiary particle beam at the first wire chamber is estimated to be less
₁₃₈ than 15 kHz. A full spill of data occurring once per supercycle is stored on the TDC
₁₃₉ board memory at once and read out by a specially designed controller. We use LVDS
₁₄₀ cables to carry both power and data between the controller and the TDCs and from

₁₄₁ the controller to the rest of the DAQ.

₁₄₂ Multi-Wire Proportional Chambers functionality

₁₄₃ We use the wire chamber system together with the bending magnets to measure the
₁₄₄ particle's momentum.

₁₄₅ In the simplest scenario, only one hit on each and every of the four wire chambers
₁₄₆ is recorded during a single readout of the detector systems. Thus, we use the hit
₁₄₇ positions in the two wire chambers upstream of the magnets to form a trajectory
₁₄₈ before the bend, and the hit positions in the two wire chambers downstream of the
₁₄₉ magnets to form a trajectory after the bend. We use the angles in the XZ plane
₁₅₀ between the upstream and downstream trajectories to calculate the Z component of
₁₅₁ the momentum as follows:

$$P_z = \frac{B_{eff}L_{eff}}{3.3(\sin(\theta_{DS}) - \sin(\theta_{US}))}, \quad (1)$$

₁₅₂ where B_{eff} is the effective maximum field in a square field approximation, L_{eff}
₁₅₃ is the effective length of both magnets (twice the effective length of one magnet),
₁₅₄ θ_{US} is the angle off the z axis of the upstream trajectory, θ_{DS} is the angle off the
₁₅₅ z axis of the downstream trajectory and $3.3 c^{-1}$ is the conversion factor from [T·m]
₁₅₆ to [MeV/c]. By using the hit positions on the third and fourth wire chamber, we
₁₅₇ estimate the azimuthal and polar angles of the particle trajectory, and we are able to
₁₅₈ calculate the other components of the momentum.

₁₅₉ The presence of multiple hits in a single wire chamber or the absence of hits in one
₁₆₀ (or more) wire chambers can complicate this simple scenario. The first complication
₁₆₁ is due to beam pile up, while the latter is due to wire chamber inefficiency. In the
₁₆₂ case of multiple hits on a single WC, at most one wire chamber track is reconstructed
₁₆₃ per event. Since the magnets bend particles only in the X direction, we assume
₁₆₄ the particle trajectory to be roughly constant in the YZ plane, thus we keep the

165 combination of hits which fit best with a straight line. It is still possible to reconstruct
166 the particle’s momentum even if the information is missing in either of the two middle
167 wire chambers (WC2 or WC3), by constraining the particle trajectory to cross the
168 plane in between the magnets.

169 Events satisfying the simplest scenario of one single hit in each of the four wire
170 chambers form the “Picky Track” sample. We construct another, higher statistics
171 sample, where we loosen the requirements on single hit and wire chamber efficiency:
172 the “High Yield” sample. For LArIAT Run II, the High Yield sample is about three
173 times the Picky Tracks statistics. For the first measurements of the LArIAT hadronic
174 cross section, we use the Picky Tracks sample because the uncertainty on the momen-
175 tum is smaller and the comparison with the beamline MC results is straightforward
176 compared with the High Yield sample; a possible future update and cross check of
177 these analysis would be the use of the High Yield sample.

178 **Four point track momentum uncertainty**

179 **0.2.3 Time-of-Flight System**

180 Two scintillator paddles, one upstream of the first set of WCs and one downstream
181 of the second set of WCs form LArIAT time-of-flight (TOF) detector system.

182 The upstream paddle is made of a 10 x 6 x 1 cm scintillator piece, read out by
183 two PMTs mounted on the beam left side which collect the light from light guides
184 mounted on all four edges of the scintillator. The downstream paddle is a 14 x 14 x
185 1 cm scintillator piece read out by two PMTs on the opposite ends of the scintillator,
186 as shown in figure 5. The relatively thin width in the beamline direction minimizes
187 energy loss of beam particles traveling through the scintillator material.

188 The CAEN 1751 digitizer is used to digitize the TOF PMTs signals at a sampling
189 rate of 1 GHz. The 12 bit samples are stored in a circular memory buffer. At trigger
190 time, data from the TOF PMTs are recorded to output in a 28.7 μ s windows starting

191 approximately 8.4 μ s before the trigger time.

192 **TOF functionality**

193 The TOF signals rise time (10-90%) is 4 ns and a full width, half-maximum of 9 ns
194 consistent in time. The signal amplitudes from the upstream TOF and downstream
195 TOF are slightly different: 200 mV for the upstream PMTs but only 50 mV for
196 downstream PMTs. The time of the pulses was calculated utilizing an oversampled
197 template derived from the data itself. We take the pulse pedestal from samples
198 far from the pulse and subtract it from the pulse amplitude. We then vertically
199 stretch a template to match the pedestal-subtracted pulse amplitude and we move
200 it horizontally to find the time. With this technique, we find a pulse time-pickoff
201 resolution better than 100 ps. The pulse pile up is not a significant problem given
202 the TOF timing resolution and the rate of the particle beam. Leveraging on the
203 pulses width uniformity of any given PMT, we flag events where two pulses overlap
204 as closely in time as 4 ns with a 90% efficiency according to simulation.

205 We combine the pulses from the two PMTs on each paddle to determine the
206 particles' arrival time by averaging the time measured from the single PMT, so to
207 minimize errors due to optical path differences in the scintillator. However, a time
208 spread of approximately 300 ps is present in both the upstream and downstream
209 detectors, likely due to transit time jitter in the PMTs themselves.

210 **0.2.4 Punch-Through and Muon Range Stack Instruments**

211 The punch-thorough and the muon range stack (MuRS) detectors are located down-
212 stream of the TPC. These detectors provide a sample of TPC crossing tracks without
213 relying on TPC information and can be used to improve particle ID for muons and
214 pions with momentum higher than 450 MeV/c.

215 The punch-thorough is simple sheet of scintillator material, read out by two PMTs.



Figure 5: Image of the down stream time of flight paddle, PMTs and relative support structure before mounting.

216 The MuRS is a segmented block of steel with four slots instrumented with scintillation
217 bars. The four steel layers in front of each instrumented slot are 2 cm, 2 cm, 14 cm
218 and 16 cm wide in the beam direction. Each instrumented slot is equipped with
219 four scintillation bars each, positioned horizontally in the direction orthogonal to the
220 beam. Each scintillator bar measures $\text{?} \times \text{?} \times 2$ cm and it is read out by one PMT.

221 The signals from both the punch-thorough and the MuRS PMTs are digitized in
222 the CAEN V1740, same as the TPC; the details of this discriminator are laid out
223 in 0.3.2. It is worth noticing that the sampling time of the CAEN V1740 is slow
224 (of the order of 128 ns), so pulse shape information from the PMT is lost. Punch-
225 thorough and MuRS hits are formed utilizing the digital discriminator signals under
226 threshold at a given time, where we obtain the threshold for each PMT directly on
227 data distributions.

228 It is worth mentioning here the presence of an additional scintillation paddle
229 between WC4 and the downstream paddle of the TOF system, called halo. The
230 halo is a $39 \times 38 \times 1$ cm 3 paddle with a 6.5 cm radius hole in the center, whose original

231 function was to reject beam particles slightly offset from the beamline center. Data
232 from this paddle turned out to be unusable, so our data events include both particle
233 going through the halo scintillation material or through the halo hole.

234 **0.2.5 LArIAT Cosmic Ray Paddle Detectors**

235 LArIAT triggers both on beam events and on cosmic rays events. We perform this
236 latter trigger by using two sets of cosmic ray paddle detectors (a.k.a. “cosmic towers”).
237 The cosmic towers frame the LArIAT cryostat, as one sits in the downstream left
238 corner and the other sits in the upstream right corner of the cryostat. Two paddle
239 sets of four scintillators pieces each make up each cosmic tower, an upper set and a
240 lower set per tower. Of the four paddles, a couple of two matched paddles stands
241 upright while the a second matched pair lies across the top of the assembly in the top
242 sets (or across the bottom of the assembly in the bottom sets). The horizontal couple
243 is used as a veto for particles traveling from inside the TPC out. The four signals
244 from the vertical paddles along one of the body diagonals of the TPC are combined
245 in a logical “AND”. This allows to select cosmic muons crossing the TPC along one
246 of its diagonals. Cosmic ray tracks crossing both anode and cathode populate the
247 events triggered this way. This particularly useful sample of tracks (which we can
248 safely assume to be associated with 5 GeV muons) can be used for many tasks; for
249 example, we use anode-cathode piercing tracks to cross check the TPC electric field
250 on data (see Appendix A), to calibrate the charge response of the TPC wires for the
251 full TPC volume and to measure the electron lifetime in the chamber [97].

252 We retrieved the scintillation paddles from the decommissioning of the CDF de-
253 tector at Fermilab and we used only the paddles with a counting efficiency greater
254 than 95% and low noise at working voltage. The measured trigger rate of the whole
255 system is 0.032 Hz, corresponding to ~ 2 muons per minute.



Figure 6: Photograph of one of the scintillation counters used in the cosmic towers.

256 0.3 In the Cryostat

257 0.3.1 Cryogenics and Argon Purity

258 LArIAT repurposed the ArgoNeuT cryostat [16] in order to use it in a beam of charged
259 particles, and added a new process piping and a new liquid argon filtration system in
260 FTBF. Inside the LArIAT experimental hall, the cryostat sits on the beam of charged
261 particles with its horizontal main axis oriented parallel to the beam.

262 Two volumes make up LArIAT cryostat, shown in Figure 7: the inner vessel and
263 the outer vessel. Purified liquid argon fills the inner vessel, while the outer volume
264 provides insulation through a vacuum jacket equipped with layers of aluminized mylar
265 superinsulation. The inner vessel is a cylinder of 130 cm length and 6.2 cm diameter,
266 containing about 550 L of LAr, corresponding to a mass of 0.76 ton. We run the
267 signal cables for the LArTPC and the high voltage feedthrough through a “chimney”
268 at the top and mid-length of the cryostat.

269 Given the different scopes of the ArgoNeuT and LArIAT detectors, we made sev-
270 eral modification to the ArgoNeuT cryostat in order to use it in LArIAT. In particular,
271 the modification shown in Figure 8 were necessary to account for the beam of charged
272 particles entering the TPC and to employ the new FTBT liquid argon purification
273 system. We added a “beam window” on the front outer end cap and an “excluder”

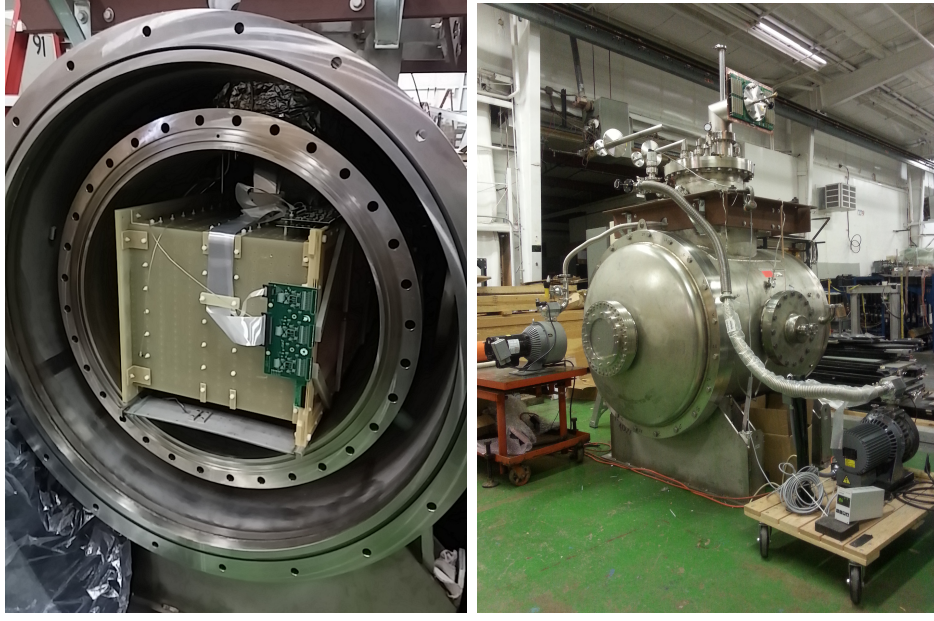


Figure 7: Left: the LArIAT TPC in the inner volume of the open cryostat. Right: cryostat fully sealed ready to be transported to FTBF.

on the inner endcap, with the scope of minimizing the amount of non-instrumented material upstream of the TPC’s active volume. The amount of non-instrumented material in front of the TPC for LArIAT corresponds to ~ 0.3 electron radiation lengths (X_0), to compare against the $\sim 1.6X_0$ of ArgoNeuT. To allow studies of the scintillation light, we added a side port feedthrough which enables the mounting of the light collection system, as well as the connections for the corresponding signal and high-voltage cables (see Section 0.3.3). We modified the bottom of the cryostat adding Conflat and ISO flange sealing to connect the liquid argon transfer line to the new argon cooling and purification system.

As in any other LArTPC, argon purity is a crucial parameter for LArIAT. Indeed, the presence of contaminants effects both the basic working principles of a LArTPC, as shown in section ???: electronegative contaminants such as oxygen and water decrease the number of ionization electrons collected on the wires after drifting through the volume. In addition, contaminants such as Nitrogen decrease the light yield from scintillation light, especially in its slow component. In LArIAT, contaminations

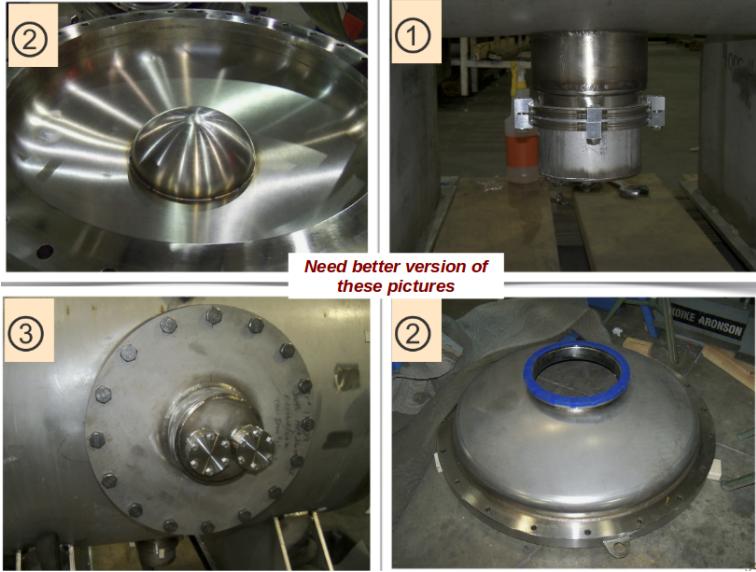


Figure 8: Main modifications to the ArgoNeuT cryostat: 1) outlet for connection to the purification system at the bottom of the cryostat; 2) the “beam-window” on the outer endcap and “excluder” which reduce the amount of non-instrumented material before the TPC; 3) the side port to host the light collection system.

should not exceed the level of 100 parts per trillion (ppt). We achieve this level of purity in several stages. The specifics required for the commercial argon bought for LArIAT are 2 parts per million (ppm) oxygen, 3.5 ppm water, and 10 ppm nitrogen. This argon is monitored with the use of commercial gas analyzer. Argon is stored in a dewar external to LArIAT hall and filtered before filling the TPC. LArIAT uses a filtration system designed for the Liquid Argon Purity Demonstrator (LAPD) [52]: half of a 77 liter filter contains a 4A molecular sieve (Sigma-Aldrich [103]) apt to remove mainly water, while the other half contains BASF CU-0226 S, a highly dispersed copper oxide impregnated on a high surface area alumina, apt to remove mainly oxygen [25]. A single pass of argon in the filter is sufficient to achieve the necessary purity, unless the filter is saturated. In case the filter saturates, the media needs to be regenerated by using heated gas; this happened twice during the Run II period¹. The filtered argon reaches the inner vessel via a liquid feedthrough on the top of the

¹. We deemed the filter regeneration necessary every time the electron lifetime dropped under 100 μ s.

302 cryostat. Argon is not recirculated in the system; rather, it boils off and vent to
303 the atmosphere. During data taking, we replenish the argon in the cryostat several
304 times per day to keep the TPC high voltage feedthrough and cold electronics always
305 submerged. In fact, we constantly monitor the level, temperature, and pressure of
306 the argon both in the commercial dewar and inside the cryostat during data taking.

307 **0.3.2 LArTPC: Charge Collection**

308 The LArIAT Liquid Argon Time Projection Chamber is a rectangular box of dimen-
309 sions 47 cm (drift) x 40 cm (height) x 90 cm (length), containing 170 liters of Liquid
310 Argon. The LArTPC three major subcomponents are

- 311 1) the cathode and field cage,
- 312 2) the wire planes,
- 313 3) the read-out electronics.

314 **Cathode and field cage**

315 A G10 plain sheet with copper metallization on one of the 40 x 90 cm inner surfaces
316 forms the cathode. A high-voltage feedthrough on the top of the LArIAT cryostat
317 delivers the high voltage to the cathode; scope of the high voltage system (Figure 9)
318 is to drift ionization electrons from the interaction of charged particles in the liquid
319 argon to the wire planes. The power supply used in this system is a Glassman
320 LX125N16 [65] capable of generating up to -125 kV and 16 mA of current, but
321 operated at -23.5kV during LArIAT Run-II. The power supply is connected via high
322 voltage cables to a series of filter pots before finally reaching the cathode.

323 The field cage is made of twenty-three parallel copper rings framing the inner walls
324 of the G10 TPC structure. A network of voltage-dividing resistors connected to the
325 field cage rings steps down the high voltage from the cathode to form a uniform electric

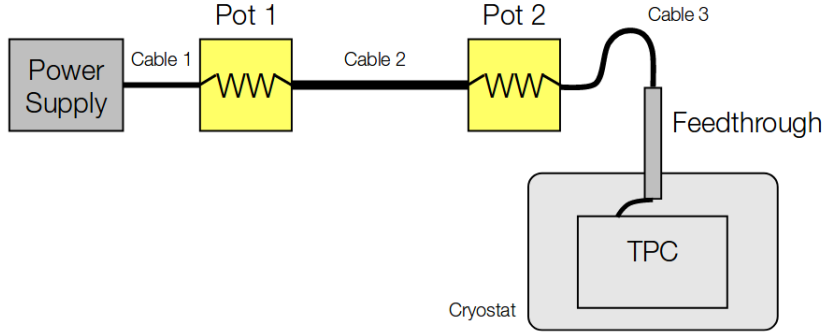


Figure 9: Schematic of the LArIAT high voltage system.

326 field. The electric field over the entire TPC drift volume is 486 V/cm, as measured
 327 in appendix A. The maximum drift length, i.e. the distance between cathode and
 328 anode planes, is 47 cm.

329 **Wire planes**

330 LArIAT counts three wire planes separated by 4 mm spaces: in order of increasing
 331 distance from the cathode, they are the shield, the induction and the collection plane.
 332 The “wire pitch”, i.e., the distance between two consecutive wires in a given plane, is
 333 4 mm. The shield plane counts 225 parallel wires of equal length oriented vertically.
 334 This plane is not connected with the read-out electronics; rather it shields the outer
 335 planes from extremely long induction signals due to the ionization chamber in the
 336 whole drift volume. As the shield plane acts almost like a Faraday cage, the shape
 337 of signals in the first instrumented plane (induction) results easier to reconstruct.
 338 Both the induction and collection planes count 240 parallel wires of different length
 339 oriented at 60° from the vertical with opposite signs. Electrons moving past the
 340 induction plane will induce a bipolar pulse on its wires; the drifting electrons will be
 341 then collected on the collection plane’s wires, forming a unipolar pulse.

342 The three wire planes and the cathode form three drift volumes, as shown in Figure
 343 10. The main drift volume is defined as the region between the cathode plane and the

344 shield plane (C-S). The other two drift regions are those between the shield plane and
 345 the induction plane (S-I), and between the induction plane and the collection plane
 346 (I-C). The electric field in these regions is chosen to satisfy the charge transparency
 347 condition and allow for 100% transmission of the drifting electrons through the shield
 348 and the induction planes.

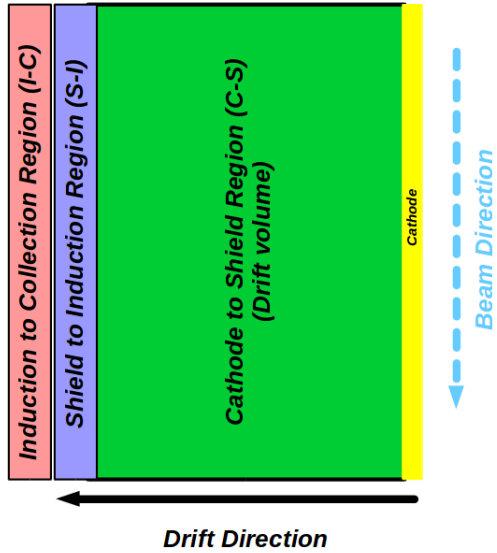


Figure 10: Schematic of the three drift regions inside the LArIAT TPC: the main drift volume between the cathode and the shield plane (C-S) in green, the region between the shield plane and the induction plane (S-I) in purple, and the region between the induction plane and the collection plane (I-C) in pink.

349 Table 1 provides the default voltages applied to the cathode and the shield, in-
 350 duction, and collection plane.

Table 1: Cathode and anode planes default voltages

Cathode	Shield	Induction	Collection
-23.17 kV	-298.8 V	-18.5 V	338.5 V

351 Electronics

352 Dedicated electronics read the induction and collection plane wires, for a total of
 353 480-channel analog signal path from the TPC wires to the signal digitizers. A digital

354 control system for the TPC-mounted electronics, a power supply, and a distribution
 355 system complete the front-end system. Figure 11 shows a block diagram of the overall
 356 system. The direct readout of the ionization electrons in liquid argon forms typically
 357 small signals on the wires, which need amplification in oder to be processed. LArIAT
 358 performs the amplification stage directly in cold with amplifiers mounted on the TPC
 359 frame inside the liquid argon, achieving a remarkable Signal-to-Noise ratio. The signal
 360 from the ASICs are driven to the other end of the readout chain, to the CAEN V1740
 361 digitizers. The CAEN V1740 has a 12 bit resolution and a maximum input range of
 362 2 VDC, resulting in about 180 ADC count for a crossing MIP.

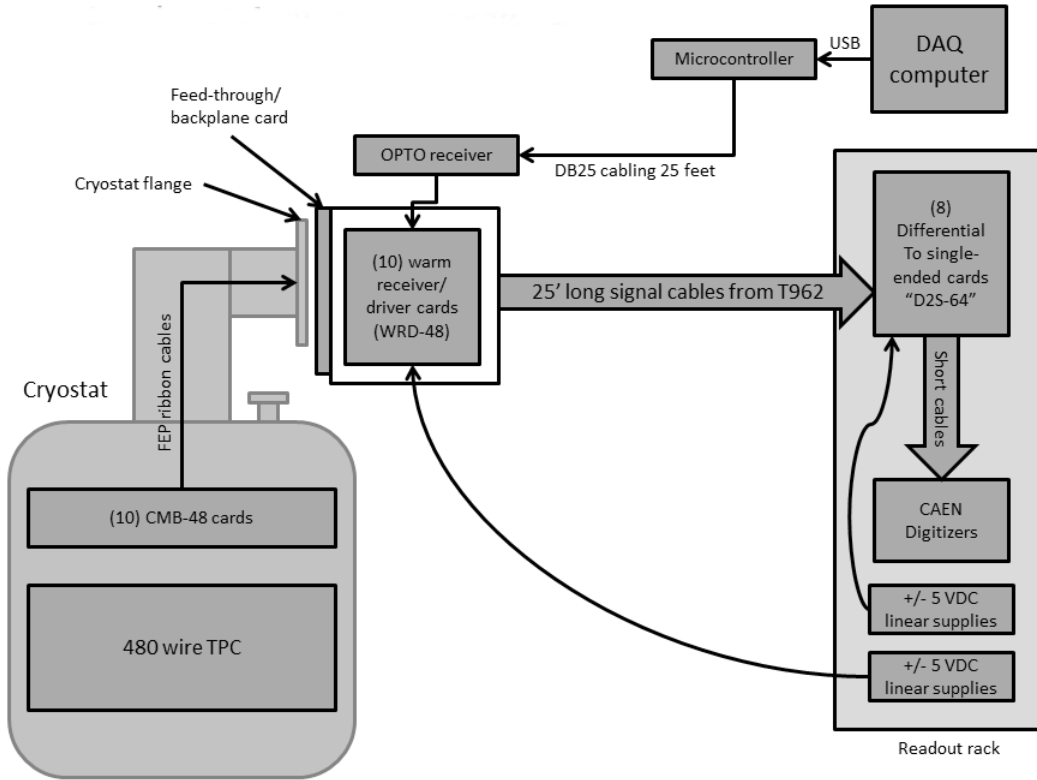


Figure 11: Overview of LArIAT Front End electronics.

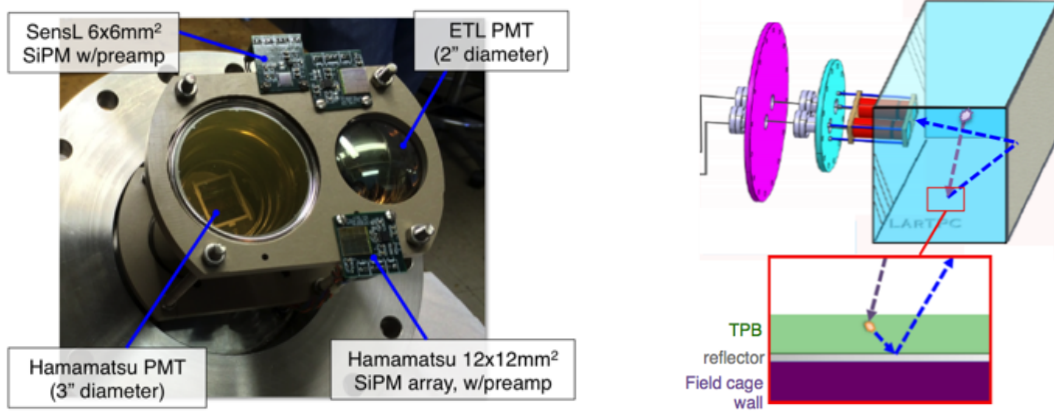


Figure 12: LArIAT’s photodetector system for observing LAr scintillation light inside the TPC (left), and a simplified schematic of VUV light being wavelength-shifting along the TPB-coated reflecting foils (right).

363 0.3.3 LArTPC: Light Collection System

364 The collection of scintillation photons is the second mechanism of particle detection
365 in argon other than the ionization electrons. Over the course of LArIAT’s three years
366 of data taking, the light collection system changed several times. We describe here
367 the light collection system for Run II. Two PMTs, a 3-inch diameter Hamamatsu
368 R-11065 and 2-inch diameter ETL D757KFL [6], as well as three SiPMs arrays (two
369 Hamamatsu S11828-3344M 4x4 arrays and one single-channel SensL MicroFB-60035)
370 are mounted on the PEEK support structure. PEEK screws into an access flange as
371 shown in Figure 12, on the anode side, leaving approximately 5 cm of clearance from
372 the collection plane.

373 Liquid argon scintillates in vacuum-ultraviolet (VUV) range at 128 nm; since cryo-
374 genic PMTs are not sensitive to VUV wavelengths, we need to shift the light in a
375 region visible to the PMTs. In LArIAT, the wavelength shifting is achieved by in-
376 stallng highly-reflective VIKUYITY dielectric substrate foils coated with a thin layer
377 of tetraphenyl-butadiene (TPB) on the four unbiased walls of the TPC . The scintil-
378 lation light interaction with the TPC emits one or more visible photons, we are then
379 reflected into the chamber. Thus, the light yield increases and results more uniform

380 across the TPC active volume, allowing the possibility of light-based calorimetry,
381 currently under study.

382 For Run II, we coated both the windows of the ETL PMT and SensL SiPM with
383 a thin layer of TPB. In doing so, some of the VUV scintillation light converts into
384 visible right at the sensor faces, keeping information on the direction of the light
385 source. Information about the light directionality is hindered for the light reflected
386 on foils, as the reflection is uniform in angle.

387 0.4 Trigger and DAQ

388 The LArIAT DAQ and trigger system governs the read out of all the many subsystems
389 forming LArIAT. The CAEN V1495 module and its user-programmable FPGA are
390 the core of this system. Every 10 ns, this module checks for matches between sixteen
391 logical inputs and user-defined patterns in the trigger menu; if it finds a match for
392 two consecutive clock ticks, that trigger fires.

393 LArIAT receives three logic signals from the Fermilab accelerator complex related
394 to the beam timing which we use as input triggers: a pulse just before the beam, a
395 pulse indicating beam-on, and a beam-off pulse.

396 The beam instruments, the cosmic ray taggers, and the light collection system
397 provide the other NIM-standard logic pulse inputs to the trigger decision. We auto-
398 matically log the trigger inputs configuration with the rest of the DAQ configuration
399 at the beginning of each run.

400 Fundamental inputs to the trigger card come from the TOF (see section 0.2.3)
401 and the wire chambers (see section 0.2.2), as activity in these systems points to the
402 presence of a charged particle in tertiary beam line. In particular, the discriminated
403 pulses from the TOF PMTs form a NIM logic pulse for the trigger logic. We ask for
404 a coincidence within a 20 ns window for all the pulses from the PMTs looking at the

405 same scintillator block and use the coincidence between the upstream and downstream
406 paddle to inform the trigger decision. In order to form a coincidence between the
407 upstream and downstream paddles, we delay the upstream paddle coincidence by
408 20 ns and widen it by 100 ns. The delay and widening are necessary to account for
409 both lightspeed particles and slower particles (high-mass) to travel the 6.5 m between
410 the upstream and the downstream paddles. For the read out of the wire chambers,
411 we use a total of sixteen multi-hit TDCs, four per chamber: two TDC per plane
412 (horizontal and vertical), sixty-four wires per TDC. In each TDC, we keep the logical
413 “OR” for any signal over threshold from the sixty-four wires. We then require a
414 coincidence between the “OR” for the horizontal TDCs and the “OR” for the vertical
415 TDCs: with this logic we make sure that at least one horizontal wire and one vertical
416 wire saw significant signal in one wire chamber. The single logical pulse from each of
417 the four wire chambers feeds into the first four inputs to the V1495 trigger card. We
418 require a coincidence within 20 ns of at least three logical inputs to form a trigger.

419 The cosmic towers (see Section 0.2.5) provide another primary input to the trigger,
420 in order to capture long tracks from cosmic muons crossing the TPC. We use NIM
421 modules to require coincidences between one upper and one lower paddle set of any
422 opposite cosmic towers. The OR all the opposite towers’ coincidences is fed as an
423 input to the trigger card.

424 We use the signal from the cryogenic PMTs (see Section 0.3.3) to form several
425 interesting triggers. The coincidence of signal from all the PMT pulses within \sim 20 ns
426 is an indication of ionizing radiation in the TPC and forms a trigger input. The
427 coincidence of two subsequent scintillation logic pulses delayed by a maximum of $7 \mu s$
428 forms the Michel electron trigger.

429 0.5 Control Systems

430 LArIAT is a complex ensemble of systems which needed to be monitored at once
431 during data taking. We performed the monitoring of the systems operations with a
432 slow control system, a DAQ monitoring system and a low level data quality monitoring
433 described in the following sections.

434 Slow Control

435 We used the Synoptic Java Web Start framework as a real-time display of subsystem
436 conditions. Its simple Graphical User Interface allowed us to change the operating
437 parameters and to graph the trends of several variables of interest for all the tertiary
438 beam detectors. Among the most important quantities monitored by Synoptic there
439 are the level of argon in both the inner vessel and the external dewar, the operating
440 voltages of cathode and wire planes, of the PMTs and SiPMs, and of the four wire
441 chambers, as well as the magnets temperature. Figure 13 shows an example of the
442 monitoring system. LArIAT uses the Accelerator Control NETwork system (ACNET)
443 to monitor the beam conditions of the MCenter beamline. For example, the horizontal
444 and vertical position of the beam at the first two wire chambers (WC1 and WC2) are
445 shown in 14 as seen by the shifter during data taking.

446 DAQ Monitoring

447 We monitor the data taking and the run time evolution with the Run Status Webpage
448 (<http://lariat-wbm.fnal.gov/lariat/run.html>), a webpage updated in real-time. The
449 page displays, among other information, the total number of triggers in the event,
450 the total number of detectors triggered during a beam spill, the trigger patterns, the
451 number of times a particular trigger pattern was satisfied during a beam spill, and
452 the current time relative to the Fermilab accelerator complex supercycle. A screen
453 shot of the page is show in figure 15.

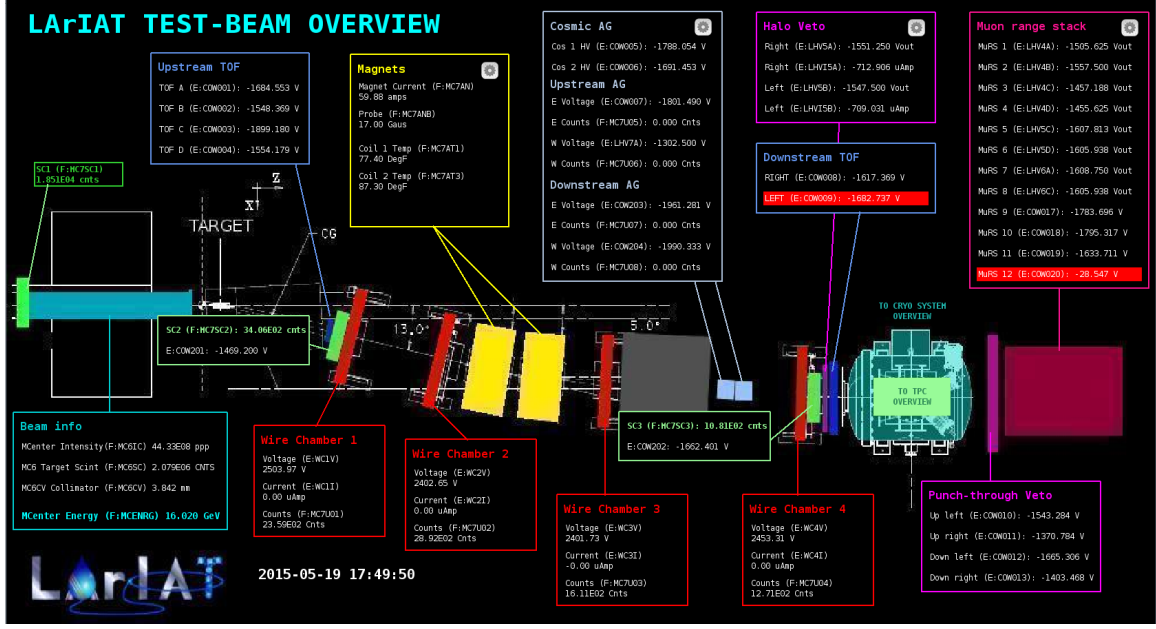


Figure 13: Interface of the Synoptic slow control system

454 Data Quality Monitoring

455 We employ two systems to ensure the quality of our data during data taking: the
 456 Near-Real-Time Data Quality Monitoring and the Event Viewer.

457 The Near-Real-Time Data Quality Monitoring (DQM) is a webpage which receives
 458 updates from all the VME boards in the trigger system and displays the results of
 459 a quick analysis of the DAQ stream of raw data on a spill-by-spill basis. The DQM
 460 allows the shifter to monitor almost in real time (typically with a 2-minute delay)
 461 a series of low level-quantities and compare them to past collections of beam spills.
 462 Some of the variables monitored in the DQM are the pedestal mean and RMS on
 463 CAEN digitizer boards of the TPC wires and PMTs of the beamline detectors, the
 464 hit occupancy and timing plots on the wire chambers, and number of data fragments
 465 recorded that are used to build a TPC event. Abnormal values for low-level quantity
 466 in the data activate a series of alarms in the DQM; this quick feedback on the DAQ
 467 and beam conditions is fundamental to assure a fast debugging of the detector and a
 468 very efficient data taking during beam uptime.

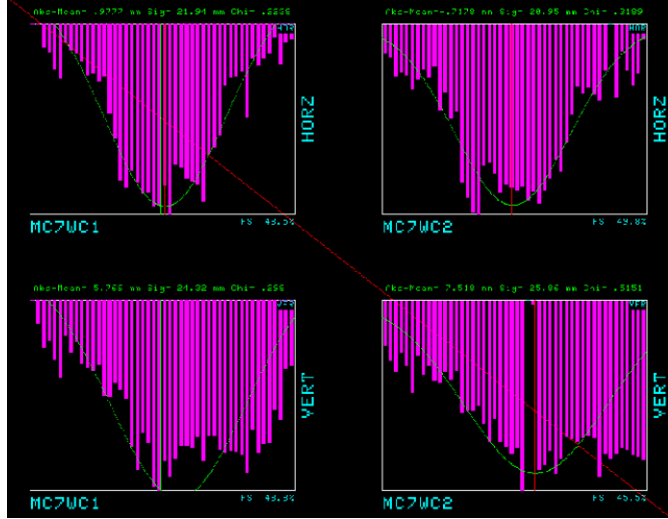


Figure 14: Beam position at the upstream wire chambers monitored with ACNET.

469 The online Event Viewer displays a two dimensional representation (Wire vs Time)
 470 of LArIAT TPC events on both the Induction and the Collection planes in near real
 471 time. The raw pulses collected by the DAQ on each wire are plotted as a function of
 472 drift time, resulting in an image of the TPC event easily readable by the shifter. This
 473 tool guarantees a particularly good check of the TPC operation which activate an
 474 immediate feedback for troubleshooting a number of issues. For example, it is easy for
 475 the shifter to spot high occupancy events and request a reduction of the primary beam
 476 intensity, or to spot a decrease of the argon purity which requires the regeneration of
 477 filters, or to catch the presence of electronic noise and reboot the ASICs. An example
 478 of high occupancy event is shown in 16.

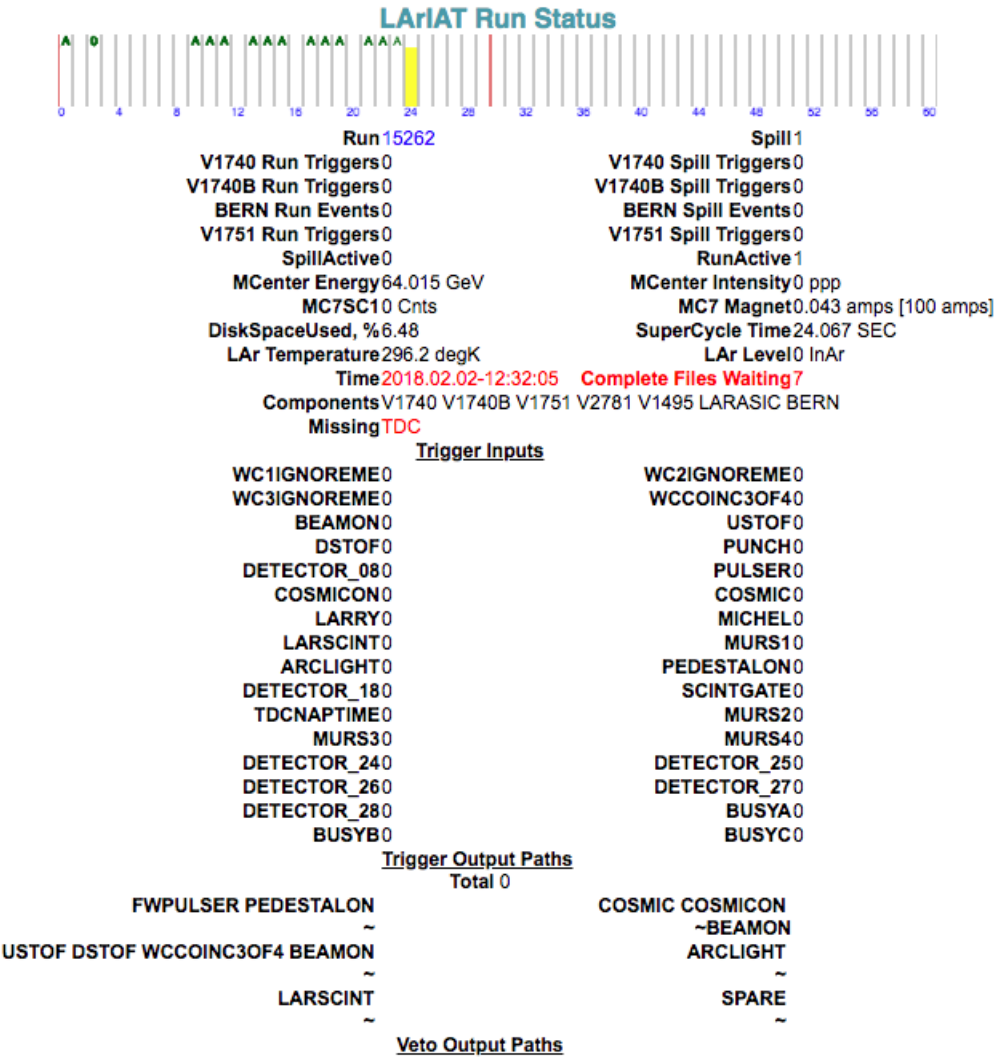


Figure 15: Run Status page at LArIAT downtime. At the top the yellow bar displays the current position in the Fermilab supercycle. Interesting information to be monitored by the shifter were the run number and number of spills, time elapsed from data taking (here in red), the energy of the secondary beam and the trigger paths.

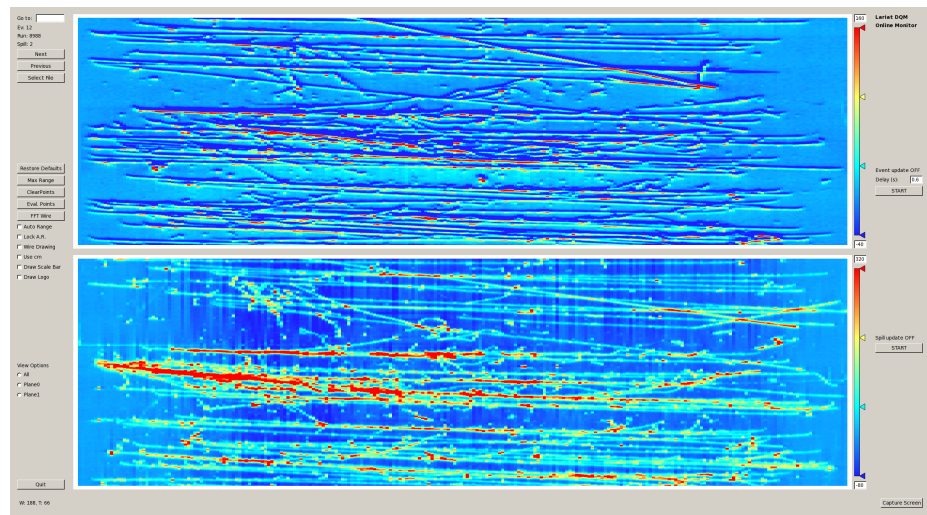


Figure 16: High occupancy event display: induction plane (top) and collection plane (bottom).

⁴⁷⁹ **Appendix A**

⁴⁸⁰ **Measurement of LArIAT Electric**
⁴⁸¹ **Field**

⁴⁸² The electric field of a LArTPC in the drift volume is a fundamental quantity for
⁴⁸³ the proper functionality of this technology, as it affects almost every reconstructed
⁴⁸⁴ quantity such as the position of hits or their collected charge. Given its importance,
⁴⁸⁵ we calculate the electric field for LArIAT with a single line diagram from our HV
⁴⁸⁶ circuit and we cross check the obtained value with a measurement relying only on
⁴⁸⁷ TPC data.

⁴⁸⁸ Before getting into the details of the measurement procedures, it is important to
⁴⁸⁹ explicit the relationship between some quantities in play. The electric field and the
⁴⁹⁰ drift velocity (v_{drift}) are related as follows

$$v_{drift} = \mu(E_{field}, T)E_{field}, \quad (\text{A.1})$$

⁴⁹¹ where μ is the electron mobility, which depends on the electric field and on the
⁴⁹² temperature (T). The empirical formula for this dependency is described in [?] and
⁴⁹³ shown in Figure A.1 for several argon temperatures.

⁴⁹⁴ The relationship between the drift time (t_{drift}) and the drift velocity is trivially

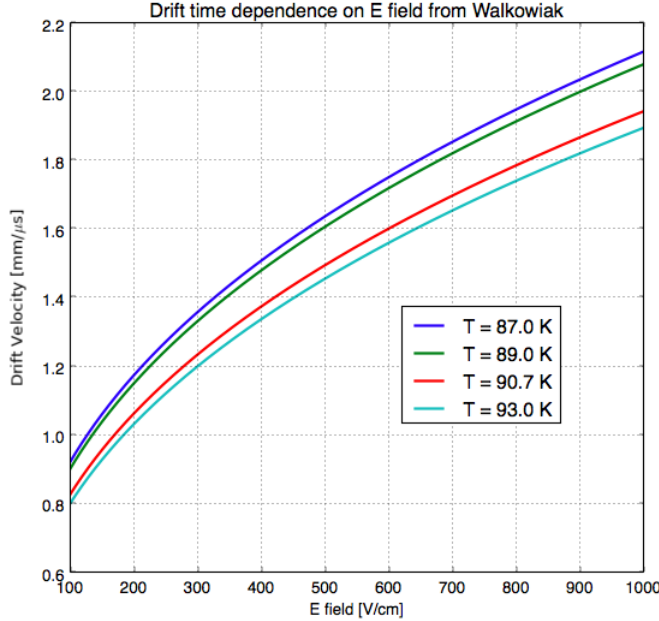


Figure A.1: Drift velocity dependence on electric field for several temperatures. The slope of the line at any one point represents the electron mobility for that given temperature and electric field.

Table A.1: Electric field and drift velocities in LArIAT smaller drift volumes

	Shield-Induction	Induction-Collection
E_{filed}	700.625 V/cm	892.5 V/cm
v_{drift}	1.73 mm/μs	1.90 mm/μs
t_{drift}	2.31 μs	2.11 μs

495 given by

$$t_{drift} = \Delta x / v_{drift}, \quad (\text{A.2})$$

496 where Δx is the distance between the edges of the drift region. Table A.1 reports the
497 values of the electric field, drift velocity, and drift times for the smaller drift volumes.

498 With these basic parameters established, we can now move on to calculating the
499 electric field in the main drift region (between the cathode and the shield plane).

500 Single line diagram method

501 The electric field strength in the LArIAT main drift volume can be determined know-
 502 ing the voltage applied to the cathode, the voltage applied at the shield plane, and the
 503 distance between them. We assume the distance between the cathode and the shield
 504 plane to be 470 mm and any length contraction due to the liquid argon is negligibly
 505 small (~ 2 mm).

506 The voltage applied to the cathode can be calculated using Ohm's law and the
 507 single line diagram shown in Figure A.2. A set of two filter pots for emergency power
 508 dissipation are positioned between the Glassman power supply and the cathode, one at
 509 each end of the feeder cable, each with an internal resistance of $40 \text{ M}\Omega$. The output
 510 current of the Glassman power supply is then used to determine the electric field
 511 strength. Figure A.3 shows an average current of 0.004172 mA from the Glassman
 512 power supply.

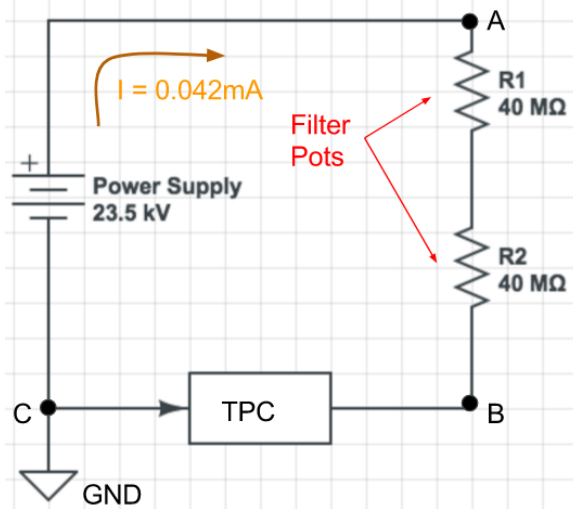


Figure A.2: get rid of current line LAr-IAT HV simple schematics.

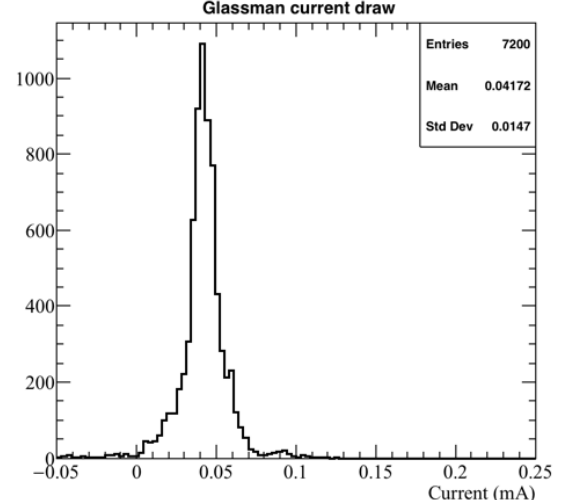


Figure A.3: **the axis is wrong!!** Current reading from the Glassman between May 25th and May 30th, 2016 (typical Run-II conditions).

513 Using this current, the voltage at the cathode is calculated as

$$V_{BC} = V_{PS} - (I \times R_{eq}) = -23.5 \text{ kV} + (0.00417 \text{ mA} \times 80 \text{ M}\Omega) = -23.17 \text{ kV}, \quad (\text{A.3})$$

514 where I is the current and R_{eq} is the equivalent resistor representing the two filter
515 pots. The electric field, drift voltage, and drift time are then calculated to be

$$E_{\text{field}} = \frac{V_{BC} - V_{\text{shield}}}{\Delta x} = 486.54 \text{ V/cm} \quad (\text{A.4})$$

516 **E field using cathode-anode piercing tracks**

517 We devise an independent method to measure the drift time (and consequently drift
518 velocity and electric field) using TPC cathode to anode piercing tracks. We use this
519 method as a cross check to the single line method. The basic idea is simple:

- 520 0. Select cosmic ray events with only 1 reconstructed track
- 521 1. Reduce the events to the one containing tracks that cross both anode and
522 cathode
- 523 2. Identify the first and last hit of the track
- 524 3. Measure the time difference between these two hits (Δt).

525 This method works under the assumptions that the time it takes for a cosmic particle
526 to cross the chamber ($\sim \text{ns}$) is small compared to the charge drift time (\sim hundreds
527 of μs).

528 We choose cosmic events to allow for a high number of anode to cathode piercing
529 tracks (ACP tracks), rejecting beam events where the particles travel almost perpen-
530 dicularly to drift direction. We select events with only one reconstructed track to
531 maximize the chance of selecting a single crossing muon (no-michel electron). We
532 utilize ACP tracks because their hits span the full drift length of the TPC, see figure

533 A.4, allowing us to define where the first and last hit of the tracks are located in space
534 regardless of our assumption of the electric field.

535 One of the main features of this method is that it doesn't rely on the measurement
536 of the trigger time. Since Δt is the time difference between the first and last hit of a
537 track and we assume the charge started drifting at the same time for both hits, the
538 measurement of the absolute beginning of drift time t_0 is unnecessary. We boost the
539 presence of ACP tracks in the cosmic sample by imposing the following requirements
540 on tracks:

- 541 • vertical position (Y) of first and last hits within ± 18 cm from TPC center
542 (avoid Top-Bottom tracks)
- 543 • horizontal position (Z) of first and last hits within 2 and 86 cm from TPC front
544 face (avoid through going tracks)
- 545 • track length greater than 48 cm (more likely to be crossing)
- 546 • angle from the drift direction (phi in figure A.5) smaller than 50 deg (more
547 reliable tracking)
- 548 • angle from the beam direction (theta in figure A.5) grater than 50 deg (more
549 reliable tracking)

550 Tracks passing all these selection requirements are used for the Δt calculation.

551 For each track passing our selection, we loop through the associated hits in order
552 to retrieve the timing information. The analysis is performed separately on hits on the
553 collection plane and induction plane, but lead to consistent results. As an example
554 of the time difference, figures A.6 and A.7 represent the difference in time between
555 the last and first hit of the selected tracks for Run-II Positive Polarity sample on the
556 collection and induction plane respectively. We fit with a Gaussian to the peak of the
557 Δt distributions to extract the mean drift time and the uncertainty associated with

558 it. The long tail at low Δt represent contamination of non-ACP tracks in the track
 559 selection. We apply the same procedure to Run-I and Run-II, positive and negative
 560 polarity alike.

561 To convert Δt recorded for the hits on the induction plane to the drift time we
 562 utilize the formula

$$t_{drift} = \Delta t - t_{S-I} \quad (\text{A.5})$$

563 where t_{drift} is the time the charge takes to drift in the main volume between the
 564 cathode and the shield plane and t_{S-I} is the time it takes for the charge to drift from
 565 the shield plane to the induction plane. In Table A.1 we calculated the drift velocity
 566 in the S-I region, thus we can calculate t_{S-I} as

$$t_{S-I} = \frac{l_{S-I}}{v_{S-I}} = \frac{4mm}{1.745mm/\mu s} \quad (\text{A.6})$$

567 where l_{S-I} is the distance between the shield and induction plane and v_{S-I} is the drift
 568 velocity in the same region. A completely analogous procedure is followed for the hits
 569 on the collection plane, taking into account the time the charge spent in drifting from
 570 shield to induction as well as between the induction and collection plane. The value
 571 for Δt_{drift} , the calculated drift velocity (v_{drift}), and corresponding drift electric field
 572 for the various run periods is given in Table A.2 and are consistent with the electric
 573 field value calculated with the single line diagram method.

Delta t_{drift} , drift v and E field with ACP tracks

Data Period	Δt_{Drift} [μs]	Drift velocity [mm/ μs]	E field [V/cm]
RunI Positive Polarity Induction	311.1 ± 2.4	1.51 ± 0.01	486.6 ± 21
RunI Positive Polarity Collection	310.9 ± 2.6	1.51 ± 0.01	487.2 ± 21
RunII Positive Polarity Induction	315.7 ± 2.8	1.49 ± 0.01	467.9 ± 21
RunII Positive Polarity Collection	315.7 ± 2.7	1.49 ± 0.01	467.9 ± 21
RunII Negative Polarity Induction	315.9 ± 2.6	1.49 ± 0.01	467.1 ± 21
RunII Negative Polarity Collection	315.1 ± 2.8	1.49 ± 0.01	470.3 ± 21
Average Values	314.1	1.50 ± 0.01	474.3 ± 21

Table A.2: Δt for the different data samples used for the Anode-Cathode Piercing tracks study.

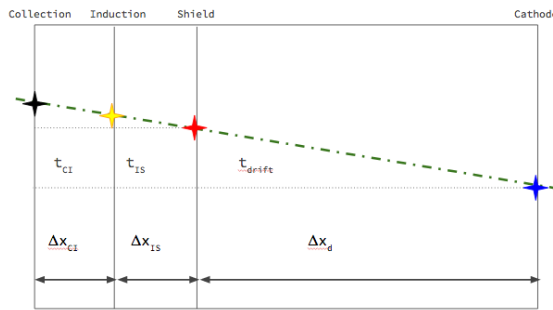


Figure A.4: Pictorial representation of the YX view of the TPC. The distance within the anode planes and between the shield plane and the cathode is purposely out of proportion to illustrate the time difference between hits on collection and induction. A ACP track is shown as an example.

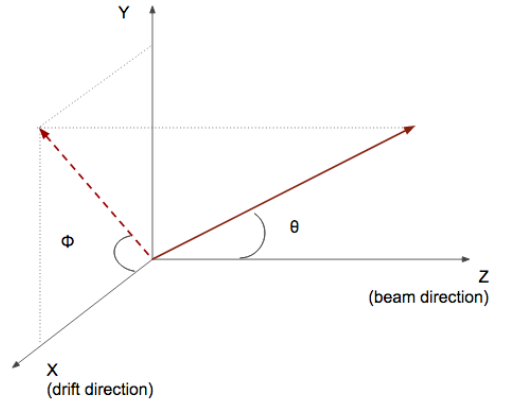


Figure A.5: Angle definition in the context of LArIAT coordinates system.

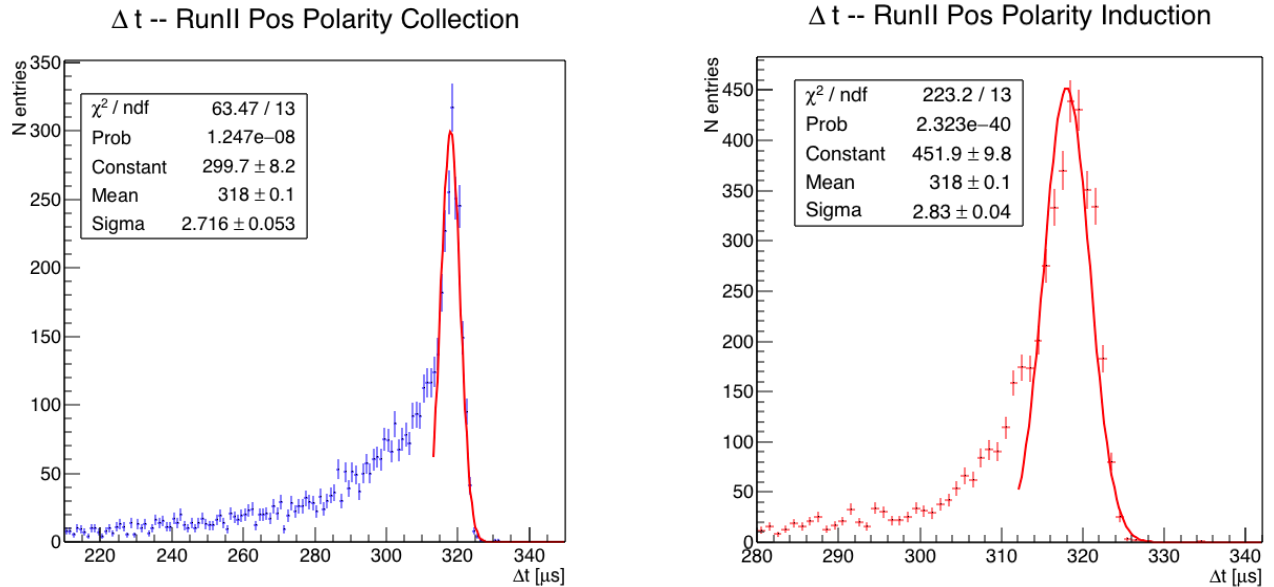


Figure A.6: Collection plane Δt fit for Run II positive polarity ACP data selected tracks.

Figure A.7: Induction plane Δt fit for Run II positive polarity ACP data selected tracks.

⁵⁷⁴ Bibliography

- ⁵⁷⁵ [1] Precision electroweak measurements on the Z resonance. *Physics Reports*,
⁵⁷⁶ 427(5):257 – 454, 2006.
- ⁵⁷⁷ [2] K. Abe, J. Amey, C. Andreopoulos, M. Antonova, S. Aoki, A. Ariga, D. Au-
⁵⁷⁸ tiero, S. Ban, M. Barbi, G. J. Barker, G. Barr, C. Barry, P. Bartet-Friburg,
⁵⁷⁹ M. Batkiewicz, V. Berardi, S. Berkman, S. Bhadra, S. Bienstock, A. Blondel,
⁵⁸⁰ S. Bolognesi, S. Bordoni, S. B. Boyd, D. Brailsford, A. Bravar, C. Bronner,
⁵⁸¹ M. Buizza Avanzini, R. G. Calland, T. Campbell, S. Cao, S. L. Cartwright,
⁵⁸² M. G. Catanesi, A. Cervera, C. Checchia, D. Cherdack, N. Chikuma,
⁵⁸³ G. Christodoulou, A. Clifton, J. Coleman, G. Collazuol, D. Coplowe, A. Cudd,
⁵⁸⁴ A. Dabrowska, G. De Rosa, T. Dealtry, P. F. Denner, S. R. Dennis, C. Densham,
⁵⁸⁵ D. Dewhurst, F. Di Lodovico, S. Di Luise, S. Dolan, O. Drapier, K. E. Duffy,
⁵⁸⁶ J. Dumarchez, M. Dziewiecki, S. Emery-Schrenk, A. Ereditato, T. Feusels,
⁵⁸⁷ A. J. Finch, G. A. Fiorentini, M. Friend, Y. Fujii, D. Fukuda, Y. Fukuda,
⁵⁸⁸ V. Galymov, A. Garcia, C. Giganti, F. Gizzarelli, T. Golan, M. Gonin, D. R.
⁵⁸⁹ Hadley, L. Haegel, M. D. Haigh, D. Hansen, J. Harada, M. Hartz, T. Hasegawa,
⁵⁹⁰ N. C. Hastings, T. Hayashino, Y. Hayato, R. L. Helmer, A. Hillairet, T. Hiraki,
⁵⁹¹ A. Hiramoto, S. Hirota, M. Hogan, J. Holeczek, F. Hosomi, K. Huang, A. K.
⁵⁹² Ichikawa, M. Ikeda, J. Imber, J. Insler, R. A. Intonti, T. Ishida, T. Ishii, E. Iwai,
⁵⁹³ K. Iwamoto, A. Izmaylov, B. Jamieson, M. Jiang, S. Johnson, P. Jonsson,
⁵⁹⁴ C. K. Jung, M. Kabirnezhad, A. C. Kabeth, T. Kajita, H. Kakuno, J. Kameda,

595 D. Karlen, T. Katori, E. Kearns, M. Khabibullin, A. Khotjantsev, H. Kim,
596 J. Kim, S. King, J. Kisiel, A. Knight, A. Knox, T. Kobayashi, L. Koch, T. Koga,
597 A. Konaka, K. Kondo, L. L. Kormos, A. Korzenev, Y. Koshio, K. Kowalik,
598 W. Kropp, Y. Kudenko, R. Kurjata, T. Kutter, J. Lagoda, I. Lamont, M. Lam-
599 oureux, E. Larkin, P. Lasorak, M. Laveder, M. Lawe, M. Licciardi, T. Lindner,
600 Z. J. Liptak, R. P. Litchfield, X. Li, A. Longhin, J. P. Lopez, T. Lou, L. Ludovici,
601 X. Lu, L. Magaletti, K. Mahn, M. Malek, S. Manly, A. D. Marino, J. F. Martin,
602 P. Martins, S. Martynenko, T. Maruyama, V. Matveev, K. Mavrokordis, W. Y.
603 Ma, E. Mazzucato, M. McCarthy, N. McCauley, K. S. McFarland, C. McGrew,
604 A. Mefodiev, C. Metelko, M. Mezzetto, P. Mijakowski, A. Minamino, O. Mi-
605 neev, S. Mine, A. Missert, M. Miura, S. Moriyama, Th. A. Mueller, J. Myslik,
606 T. Nakadaira, M. Nakahata, K. G. Nakamura, K. Nakamura, K. D. Nakamura,
607 Y. Nakanishi, S. Nakayama, T. Nakaya, K. Nakayoshi, C. Nantais, C. Nielsen,
608 M. Nirko, K. Nishikawa, Y. Nishimura, P. Novella, J. Nowak, H. M. O'Keeffe,
609 K. Okumura, T. Okusawa, W. Oryszczak, S. M. Oser, T. Ovsyannikova, R. A.
610 Owen, Y. Oyama, V. Palladino, J. L. Palomino, V. Paolone, N. D. Patel,
611 P. Paudyal, M. Pavin, D. Payne, J. D. Perkin, Y. Petrov, L. Pickard, L. Pick-
612 ering, E. S. Pinzon Guerra, C. Pistillo, B. Popov, M. Posiadala-Zezula, J.-M.
613 Poutissou, R. Poutissou, P. Przewlocki, B. Quilain, T. Radermacher, E. Radi-
614 cioni, P. N. Ratoff, M. Ravonel, M. A. Rayner, A. Redij, E. Reinherz-Aronis,
615 C. Riccio, P. A. Rodrigues, E. Rondio, B. Rossi, S. Roth, A. Rubbia, A. Rychter,
616 K. Sakashita, F. Sánchez, E. Scantamburlo, K. Scholberg, J. Schwehr, M. Scott,
617 Y. Seiya, T. Sekiguchi, H. Sekiya, D. Sgalaberna, R. Shah, A. Shaikhiev,
618 F. Shaker, D. Shaw, M. Shiozawa, T. Shirahige, S. Short, M. Smy, J. T.
619 Sobczyk, H. Sobel, M. Sorel, L. Southwell, J. Steinmann, T. Stewart, P. Stowell,
620 Y. Suda, S. Suvorov, A. Suzuki, S. Y. Suzuki, Y. Suzuki, R. Tacik, M. Tada,
621 A. Takeda, Y. Takeuchi, H. K. Tanaka, H. A. Tanaka, D. Terhorst, R. Terri,

- 622 T. Thakore, L. F. Thompson, S. Tobayama, W. Toki, T. Tomura, C. Touramanis,
 623 T. Tsukamoto, M. Tzanov, Y. Uchida, M. Vagins, Z. Vallari, G. Vasseur,
 624 T. Vladislavljevic, T. Wachala, C. W. Walter, D. Wark, M. O. Wascko, A. Weber,
 625 R. Wendell, R. J. Wilkes, M. J. Wilking, C. Wilkinson, J. R. Wilson, R. J.
 626 Wilson, C. Wret, Y. Yamada, K. Yamamoto, M. Yamamoto, C. Yanagisawa,
 627 T. Yano, S. Yen, N. Yershov, M. Yokoyama, K. Yoshida, T. Yuan, M. Yu, A. Za-
 628 lewska, J. Zalipska, L. Zambelli, K. Zaremba, M. Ziembicki, E. D. Zimmerman,
 629 M. Zito, and J. Źmuda. Combined analysis of neutrino and antineutrino oscil-
 630 lations at t2k. *Phys. Rev. Lett.*, 118:151801, Apr 2017.
- 631 [3] K. Abe, Y. Haga, Y. Hayato, M. Ikeda, K. Iyogi, J. Kameda, Y. Kishimoto,
 632 M. Miura, S. Moriyama, M. Nakahata, T. Nakajima, Y. Nakano, S. Nakayama,
 633 A. Orii, H. Sekiya, M. Shiozawa, A. Takeda, H. Tanaka, T. Tomura, R. A. Wen-
 634 dell, R. Akutsu, T. Irvine, T. Kajita, K. Kaneyuki, Y. Nishimura, E. Richard,
 635 K. Okumura, L. Labarga, P. Fernandez, J. Gustafson, C. Kachulis, E. Kearns,
 636 J. L. Raaf, J. L. Stone, L. R. Sulak, S. Berkman, C. M. Nantais, H. A.
 637 Tanaka, S. Tobayama, M. Goldhaber, W. R. Kropp, S. Mine, P. Weatherly,
 638 M. B. Smy, H. W. Sobel, V. Takhistov, K. S. Ganezer, B. L. Hartfiel, J. Hill,
 639 N. Hong, J. Y. Kim, I. T. Lim, R. G. Park, A. Himmel, Z. Li, E. O’Sullivan,
 640 K. Scholberg, C. W. Walter, T. Wongjirad, T. Ishizuka, S. Tasaka, J. S. Jang,
 641 J. G. Learned, S. Matsuno, S. N. Smith, M. Friend, T. Hasegawa, T. Ishida,
 642 T. Ishii, T. Kobayashi, T. Nakadaira, K. Nakamura, Y. Oyama, K. Sakashita,
 643 T. Sekiguchi, T. Tsukamoto, A. T. Suzuki, Y. Takeuchi, T. Yano, S. V. Cao,
 644 T. Hiraki, S. Hirota, K. Huang, T. Kikawa, A. Minamino, T. Nakaya, K. Suzuki,
 645 Y. Fukuda, K. Choi, Y. Itow, T. Suzuki, P. Mijakowski, K. Frankiewicz, J. Hig-
 646 night, J. Imber, C. K. Jung, X. Li, J. L. Palomino, M. J. Wilking, C. Yanag-
 647 isawa, D. Fukuda, H. Ishino, T. Kayano, A. Kibayashi, Y. Koshio, T. Mori,
 648 M. Sakuda, C. Xu, Y. Kuno, R. Tacik, S. B. Kim, H. Okazawa, Y. Choi,

- 649 K. Nishijima, M. Koshiba, Y. Totsuka, Y. Suda, M. Yokoyama, C. Bronner,
650 M. Hartz, K. Martens, Ll. Marti, Y. Suzuki, M. R. Vagins, J. F. Martin, A. Kon-
651 aka, S. Chen, Y. Zhang, and R. J. Wilkes. Search for proton decay via $p \rightarrow e^+ \pi^0$
652 and $p \rightarrow \mu^+ \pi^0$ in 0.31 megaton·years exposure of the super-kamiokande water
653 cherenkov detector. *Phys. Rev. D*, 95:012004, Jan 2017.
- 654 [4] R Acciarri, C Adams, J Asaadi, B Baller, T Bolton, C Bromberg, F Ca-
655 vanna, E Church, D Edmunds, A Ereditato, S Farooq, B Fleming, H Greenlee,
656 G Horton-Smith, C James, E Klein, K Lang, P Laurens, D McKee, R Mehdiyev,
657 B Page, O Palamara, K Partyka, G Rameika, B Rebel, M Soderberg, J Spitz,
658 A M Szelc, M Weber, M Wojcik, T Yang, and G P Zeller. A study of electron
659 recombination using highly ionizing particles in the argoneut liquid argon tpc.
660 *Journal of Instrumentation*, 8(08):P08005, 2013.
- 661 [5] R Acciarri, M Antonello, B Baibussinov, M Baldo-Ceolin, P Benetti,
662 F Calaprice, E Calligarich, M Cambiaghi, N Canci, F Carbonara, F Cavanna,
663 S Centro, A G Cocco, F Di Pompeo, G Fiorillo, C Galbiati, V Gallo, L Grandi,
664 G Meng, I Modena, C Montanari, O Palamara, L Pandola, G B Piano Mortari,
665 F Pietropaolo, G L Raselli, M Roncadelli, M Rossella, C Rubbia, E Segreto,
666 A M Szelc, S Ventura, and C Vignoli. Effects of nitrogen contamination in
667 liquid argon. *Journal of Instrumentation*, 5(06):P06003, 2010.
- 668 [6] R. Acciarri et al. Demonstration and Comparison of Operation of Photomulti-
669 plier Tubes at Liquid Argon Temperature. *JINST*, 7:P01016, 2012.
- 670 [7] R. Acciarri et al. Design and Construction of the MicroBooNE Detector. *JINST*,
671 12(02):P02017, 2017.
- 672 [8] R. Acciarri et al. First Observation of Low Energy Electron Neutrinos in a
673 Liquid Argon Time Projection Chamber. *Phys. Rev.*, D95(7):072005, 2017.

- 674 [Phys. Rev.D95,072005(2017)].
- 675 [9] M Adamowski, B Carls, E Dvorak, A Hahn, W Jaskierny, C Johnson, H Jostlein,
676 C Kendziora, S Lockwitz, B Pahlka, R Plunkett, S Pordes, B Rebel, R Schmitt,
677 M Stancari, T Tope, E Voirin, and T Yang. The liquid argon purity demon-
678 strator. *Journal of Instrumentation*, 9(07):P07005, 2014.
- 679 [10] C. Adams et al. The Long-Baseline Neutrino Experiment: Exploring Funda-
680 mental Symmetries of the Universe. 2013.
- 681 [11] P. Adamson, L. Aliaga, D. Ambrose, N. Anfimov, A. Antoshkin, E. Arrieta-
682 Diaz, K. Augsten, A. Aurisano, C. Backhouse, M. Baird, B. A. Bambah,
683 K. Bays, B. Behera, S. Bending, R. Bernstein, V. Bhatnagar, B. Bhuyan,
684 J. Bian, T. Blackburn, A. Bolshakova, C. Bromberg, J. Brown, G. Brunetti,
685 N. Buchanan, A. Butkevich, V. Bychkov, M. Campbell, E. Catano-Mur, S. Chil-
686 dress, B. C. Choudhary, B. Chowdhury, T. E. Coan, J. A. B. Coelho, M. Colo,
687 J. Cooper, L. Corwin, L. Cremonesi, D. Cronin-Hennessy, G. S. Davies, J. P.
688 Davies, P. F. Derwent, R. Dharmapalan, P. Ding, Z. Djurcic, E. C. Dukes,
689 H. Duyang, S. Edayath, R. Ehrlich, G. J. Feldman, M. J. Frank, M. Gabrielyan,
690 H. R. Gallagher, S. Germani, T. Ghosh, A. Giri, R. A. Gomes, M. C. Goodman,
691 V. Grichine, R. Group, D. Grover, B. Guo, A. Habig, J. Hartnell, R. Hatcher,
692 A. Hatzikoutelis, K. Heller, A. Himmel, A. Holin, J. Hylen, F. Jediny, M. Judah,
693 G. K. Kafka, D. Kalra, S. M. S. Kasahara, S. Kasetti, R. Keloth, L. Kolupaeva,
694 S. Kotelnikov, I. Kourbanis, A. Kreymer, A. Kumar, S. Kurbanov, K. Lang,
695 W. M. Lee, S. Lin, J. Liu, M. Lokajicek, J. Lozier, S. Luchuk, K. Maan, S. Mag-
696 ill, W. A. Mann, M. L. Marshak, K. Matera, V. Matveev, D. P. Méndez, M. D.
697 Messier, H. Meyer, T. Miao, W. H. Miller, S. R. Mishra, R. Mohanta, A. Moren,
698 L. Mualem, M. Muether, S. Mufson, R. Murphy, J. Musser, J. K. Nelson,
699 R. Nichol, E. Niner, A. Norman, T. Nosek, Y. Oksuzian, A. Olshevskiy, T. Ol-

700 son, J. Paley, P. Pandey, R. B. Patterson, G. Pawloski, D. Pershey, O. Petrova,
701 R. Petti, S. Phan-Budd, R. K. Plunkett, R. Poling, B. Potukuchi, C. Principato,
702 F. Psihas, A. Radovic, R. A. Rameika, B. Rebel, B. Reed, D. Rocco, P. Rojas,
703 V. Ryabov, K. Sachdev, P. Sail, O. Samoylov, M. C. Sanchez, R. Schroeter,
704 J. Sepulveda-Quiroz, P. Shanahan, A. Sheshukov, J. Singh, J. Singh, P. Singh,
705 V. Singh, J. Smolik, N. Solomey, E. Song, A. Sousa, K. Soustruznik, M. Strait,
706 L. Suter, R. L. Talaga, M. C. Tamsett, P. Tas, R. B. Thayyullathil, J. Thomas,
707 X. Tian, S. C. Tognini, J. Tripathi, A. Tsaris, J. Urheim, P. Vahle, J. Vasel,
708 L. Vinton, A. Vold, T. Vrba, B. Wang, M. Wetstein, D. Whittington, S. G. Wo-
709 jcicki, J. Wolcott, N. Yadav, S. Yang, J. Zalesak, B. Zamorano, and R. Zwaska.
710 Constraints on oscillation parameters from ν_e appearance and ν_μ disappearance
711 in nova. *Phys. Rev. Lett.*, 118:231801, Jun 2017.

712 [12] Alan Agresti. *Categorical Data Analysis*. Wiley Series in Probability and Statis-
713 tics. Wiley, 2013.

714 [13] A. Aguilar-Arevalo et al. Evidence for neutrino oscillations from the observation
715 of anti-neutrino(electron) appearance in a anti-neutrino(muon) beam. *Phys.*
716 *Rev.*, D64:112007, 2001.

717 [14] A. A. Aguilar-Arevalo et al. Improved Search for $\bar{\nu}_\mu \rightarrow \bar{\nu}_e$ Oscillations in the
718 MiniBooNE Experiment. *Phys. Rev. Lett.*, 110:161801, 2013.

719 [15] S. Amoruso et al. Study of electron recombination in liquid argon with the
720 ICARUS TPC. *Nucl. Instrum. Meth.*, A523:275–286, 2004.

721 [16] C. Anderson et al. The ArgoNeuT Detector in the NuMI Low-Energy beam
722 line at Fermilab. *JINST*, 7:P10019, 2012.

723 [17] C. Andreopoulos et al. The GENIE Neutrino Monte Carlo Generator. *Nucl.*
724 *Instrum. Meth.*, A614:87–104, 2010.

- 725 [18] M. Antonello, B. Baibussinov, P. Benetti, E. Calligarich, N. Canci, S. Centro,
726 A. Cesana, K. Cieslik, D. B. Cline, A. G. Cocco, A. Dabrowska, D. De-
727 qual, A. Dermenev, R. Dolfini, C. Farnese, A. Fava, A. Ferrari, G. Fiorillo,
728 D. Gibin, S. Gninenko, A. Guglielmi, M. Haranczyk, J. Holeczek, A. Ivashkin,
729 J. Kisiel, I. Kochanek, J. Lagoda, S. Mania, A. Menegolli, G. Meng, C. Monta-
730 nari, S. Otwinowski, A. Piazzoli, P. Picchi, F. Pietropaolo, P. Plonski, A. Rap-
731 poldi, G. L. Raselli, M. Rossella, C. Rubbia, P. Sala, A. Scaramelli, E. Seg-
732 reto, F. Sergiampietri, D. Stefan, J. Stepaniak, R. Sulej, M. Szarska, M. Ter-
733 rani, F. Varanini, S. Ventura, C. Vignoli, H. Wang, X. Yang, A. Zalewska,
734 and K. Zaremba. Precise 3d track reconstruction algorithm for the ICARUS
735 t600 liquid argon time projection chamber detector. *Advances in High Energy
Physics*, 2013:1–16, 2013.
- 737 [19] M. Antonello et al. A Proposal for a Three Detector Short-Baseline Neutrino
738 Oscillation Program in the Fermilab Booster Neutrino Beam. 2015.
- 739 [20] D. Ashery, I. Navon, G. Azuelos, H. K. Walter, H. J. Pfeiffer, and F. W.
740 Schlepütz. True absorption and scattering of pions on nuclei. *Phys. Rev. C*,
741 23:2173–2185, May 1981.
- 742 [21] C. Athanassopoulos et al. Evidence for $\nu(\mu) \rightarrow \nu(e)$ neutrino oscillations
743 from LSND. *Phys. Rev. Lett.*, 81:1774–1777, 1998.
- 744 [22] Borut Bajc, Junji Hisano, Takumi Kuwahara, and Yuji Omura. Threshold
745 corrections to dimension-six proton decay operators in non-minimal {SUSY}
746 $\text{su}(5)$ {GUTs}. *Nuclear Physics B*, 910:1 – 22, 2016.
- 747 [23] B. Baller. Trajcluster user guide. Technical report, apr 2016.
- 748 [24] Gary Barker. Neutrino event reconstruction in a liquid argon TPC. *Journal of
749 Physics: Conference Series*, 308:012015, jul 2011.

- 750 [25] BASF Corp. 100 Park Avenue, Florham Park, NJ 07932 USA.
- 751 [26] R. Becker-Szendy, C. B. Bratton, D. R. Cady, D. Casper, R. Claus, M. Crouch,
752 S. T. Dye, W. Gajewski, M. Goldhaber, T. J. Haines, P. G. Halverson, T. W.
753 Jones, D. Kielczewska, W. R. Kropp, J. G. Learned, J. M. LoSecco, C. Mc-
754 Grew, S. Matsuno, J. Matthews, M. S. Mudah, L. Price, F. Reines, J. Schultz,
755 D. Sinclair, H. W. Sobel, J. L. Stone, L. R. Sulak, R. Svoboda, G. Thornton,
756 and J. C. van der Velde. Search for proton decay into $e^+ + \pi^0$ in the imb-3
757 detector. *Phys. Rev. D*, 42:2974–2976, Nov 1990.
- 758 [27] J B Birks. Scintillations from organic crystals: Specific fluorescence and relative
759 response to different radiations. *Proceedings of the Physical Society. Section A*,
760 64(10):874, 1951.
- 761 [28] A. Bodek and J. L. Ritchie. Further studies of fermi-motion effects in lepton
762 scattering from nuclear targets. *Phys. Rev. D*, 24:1400–1402, Sep 1981.
- 763 [29] Mark G. Boulay and A. Hime. Direct WIMP detection using scintillation time
764 discrimination in liquid argon. 2004.
- 765 [30] D. V. Bugg, R. S. Gilmore, K. M. Knight, D. C. Salter, G. H. Stafford, E. J. N.
766 Wilson, J. D. Davies, J. D. Dowell, P. M. Hattersley, R. J. Homer, A. W. O'dell,
767 A. A. Carter, R. J. Tapper, and K. F. Riley. Kaon-nucleon total cross sections
768 from 0.6 to 2.65 gev/ *c*. *Phys. Rev.*, 168:1466–1475, Apr 1968.
- 769 [31] W. M. Burton and B. A. Powell. Fluorescence of tetraphenyl-butadiene in the
770 vacuum ultraviolet. *Applied Optics*, 12(1):87, jan 1973.
- 771 [32] A. S. Carroll, I. H. Chiang, C. B. Dover, T. F. Kycia, K. K. Li, P. O. Mazur,
772 D. N. Michael, P. M. Mockett, D. C. Rahm, and R. Rubinstein. Pion-nucleus
773 total cross sections in the (3,3) resonance region. *Phys. Rev. C*, 14:635–638,
774 Aug 1976.

- 775 [33] D. Casper. The nuance neutrino physics simulation, and the future. *Nuclear*
776 *Physics B - Proceedings Supplements*, 112(1-3):161–170, nov 2002.
- 777 [34] A. Cervera, A. Donini, M.B. Gavela, J.J. Gomez Cádenas, P. Hernández,
778 O. Mena, and S. Rigolin. Golden measurements at a neutrino factory. *Nu-*
779 *nuclear Physics B*, 579(1-2):17–55, jul 2000.
- 780 [35] E. Church. LArSoft: A Software Package for Liquid Argon Time Projection
781 Drift Chambers. 2013.
- 782 [36] ATLAS Collaboration. Observation of a new particle in the search for the
783 standard model higgs boson with the ATLAS detector at the LHC. *Physics*
784 *Letters B*, 716(1):1–29, sep 2012.
- 785 [37] CMS Collaboration. Observation of a new boson at a mass of 125 gev with the
786 cms experiment at the lhc. *Physics Letters B*, 716(1):30 – 61, 2012.
- 787 [38] The LArIAT Collaboration. The liquid argon in a testbeam (lariat) experiment.
788 Technical report, In Preparation 2018.
- 789 [39] Stefano Dell’Oro, Simone Marcocci, Matteo Viel, and Francesco Vissani. Neu-
790 trinoless double beta decay: 2015 review. *Advances in High Energy Physics*,
791 2016:1–37, 2016.
- 792 [40] S.E. Derenzo, A.R. Kirschbaum, P.H. Eberhard, R.R. Ross, and F.T. Solmitz.
793 Test of a liquid argon chamber with 20 m rms resolution. *Nuclear Instruments*
794 *and Methods*, 122:319 – 327, 1974.
- 795 [41] Savas Dimopoulos, Stuart Raby, and Frank Wilczek. Proton Decay in Super-
796 symmetric Models. *Phys. Lett.*, B112:133, 1982.
- 797 [42] D. Drakoulakos et al. Proposal to perform a high-statistics neutrino scattering
798 experiment using a fine-grained detector in the NuMI beam. 2004.

- 799 [43] A Ereditato, C C Hsu, S Janos, I Kreslo, M Messina, C Rudolf von Rohr,
800 B Rossi, T Strauss, M S Weber, and M Zeller. Design and operation of
801 argontube: a 5 m long drift liquid argon tpc. *Journal of Instrumentation*,
802 8(07):P07002, 2013.
- 803 [44] Torleif Ericson and Wolfram Weise. *Pions and Nuclei (The International Series*
804 *of Monographs on Physics)*. Oxford University Press, 1988.
- 805 [45] A.A. Aguilar-Arevalo et al. The miniboone detector. *Nuclear Instruments and*
806 *Methods in Physics Research Section A: Accelerators, Spectrometers, Detectors*
807 *and Associated Equipment*, 599(1):28 – 46, 2009.
- 808 [46] Antonio Bueno et al. Nucleon decay searches with large liquid argon TPC de-
809 tectors at shallow depths: atmospheric neutrinos and cosmogenic backgrounds.
810 *Journal of High Energy Physics*, 2007(04):041–041, apr 2007.
- 811 [47] A.S. Clough et al. Pion-nucleus total cross sections from 88 to 860 MeV. *Nuclear*
812 *Physics B*, 76(1):15–28, jul 1974.
- 813 [48] B.W. Allardyce et al. Pion reaction cross sections and nuclear sizes. *Nuclear*
814 *Physics A*, 209(1):1 – 51, 1973.
- 815 [49] C Athanassopoulos et al. The liquid scintillator neutrino detector and LAMPF
816 neutrino source. *Nuclear Instruments and Methods in Physics Research Section*
817 *A: Accelerators, Spectrometers, Detectors and Associated Equipment*, 388(1-
818 2):149–172, mar 1997.
- 819 [50] F. Binon et al. Scattering of negative pions on carbon. *Nuclear Physics B*,
820 17(1):168 – 188, 1970.
- 821 [51] L. Aliaga et al. Minerva neutrino detector response measured with test beam
822 data. *Nuclear Instruments and Methods in Physics Research Section A: Ac-*

- 823 *celerators, Spectrometers, Detectors and Associated Equipment*, 789:28 – 42,
824 2015.
- 825 [52] M Adamowski et al. The liquid argon purity demonstrator. *Journal of Instru-*
826 *mentation*, 9(07):P07005, 2014.
- 827 [53] P. Vilain et al. Coherent single charged pion production by neutrinos. *Physics*
828 *Letters B*, 313(1-2):267–275, aug 1993.
- 829 [54] R. Acciarri et al. Convolutional neural networks applied to neutrino events
830 in a liquid argon time projection chamber. *Journal of Instrumentation*,
831 12(03):P03011, 2017.
- 832 [55] R. Acciarri et al. Design and construction of the MicroBooNE detector. *Journal*
833 *of Instrumentation*, 12(02):P02017–P02017, feb 2017.
- 834 [56] C. E. Aalseth et al.l. DarkSide-20k: A 20 tonne two-phase LAr TPC for direct
835 dark matter detection at LNGS. *The European Physical Journal Plus*, 133(3),
836 mar 2018.
- 837 [57] H Fenker. Standard beam pwc for fermilab. Technical report, Fermi National
838 Accelerator Lab., Batavia, IL (USA), 1983.
- 839 [58] H Fesbach. Theoretical nuclear physics: Nuclear reactions. 1992.
- 840 [59] J. A. Formaggio and G. P. Zeller. From ev to eev: Neutrino cross sections across
841 energy scales. *Rev. Mod. Phys.*, 84:1307–1341, Sep 2012.
- 842 [60] E. Friedman et al. K+ nucleus reaction and total cross-sections: New analysis
843 of transmission experiments. *Phys. Rev.*, C55:1304–1311, 1997.
- 844 [61] V.M. Gehman, S.R. Seibert, K. Rielage, A. Hime, Y. Sun, D.-M. Mei,
845 J. Maassen, and D. Moore. Fluorescence efficiency and visible re-emission

- 846 spectrum of tetraphenyl butadiene films at extreme ultraviolet wavelengths.
847 *Nuclear Instruments and Methods in Physics Research Section A: Accelerators,*
848 *Spectrometers, Detectors and Associated Equipment*, 654(1):116 – 121, 2011.
- 849 [62] H. Geiger and E. Marsden. On a diffuse reflection of the formula-particles.
850 *Proceedings of the Royal Society A: Mathematical, Physical and Engineering*
851 *Sciences*, 82(557):495–500, jul 1909.
- 852 [63] Howard Georgi and S. L. Glashow. Unity of all elementary-particle forces. *Phys.*
853 *Rev. Lett.*, 32:438–441, Feb 1974.
- 854 [64] D.Y. Wong (editor) G.L. Shaw (Editor). *Pion-nucleon Scattering*. John Wiley
855 & Sons Inc, 1969.
- 856 [65] Glassman High Voltage, Inc., Precision Regulated High Voltage DC Power Sup-
857 ply.
- 858 [66] D S Gorbunov. Sterile neutrinos and their role in particle physics and cosmology.
859 *Physics-Uspekhi*, 57(5):503, 2014.
- 860 [67] C. Green, J. Kowalkowski, M. Paterno, M. Fischler, L. Garren, and Q. Lu. The
861 Art Framework. *J. Phys. Conf. Ser.*, 396:022020, 2012.
- 862 [68] S. Hansen, D. Jensen, G. Savage, E. Skup, and A. Soha. Fermilab test beam
863 multi-wire proportional chamber tracking system upgrade. June 2014. Interna-
864 tional Conference on Technology and Instrumentation in Particle Physics (TIPP
865 2014).
- 866 [69] J. Harada. Non-maximal θ_{23} , large θ_{13} and tri-bimaximal θ_{12} via quark-
867 lepton complementarity at next-to-leading order. *EPL (Europhysics Letters)*,
868 103(2):21001, 2013.

- 869 [70] Peter W. Higgs. Broken symmetries and the masses of gauge bosons. *Physical*
870 *Review Letters*, 13(16):508–509, oct 1964.
- 871 [71] P.W. Higgs. Broken symmetries, massless particles and gauge fields. *Physics*
872 *Letters*, 12(2):132–133, sep 1964.
- 873 [72] H J Hilke. Time projection chambers. *Reports on Progress in Physics*,
874 73(11):116201, 2010.
- 875 [73] N. Ishida, M. Chen, T. Doke, K. Hasuike, A. Hitachi, M. Gaudreau, M. Kase,
876 Y. Kawada, J. Kikuchi, T. Komiyama, K. Kuwahara, K. Masuda, H. Okada,
877 Y.H. Qu, M. Suzuki, and T. Takahashi. Attenuation length measurements of
878 scintillation light in liquid rare gases and their mixtures using an improved
879 reflection suppresser. *Nuclear Instruments and Methods in Physics Research*
880 *Section A: Accelerators, Spectrometers, Detectors and Associated Equipment*,
881 384(2-3):380–386, jan 1997.
- 882 [74] George Jaffé. Zur theorie der ionisation in kolonnen. *Annalen der Physik*,
883 347(12):303–344, 1913.
- 884 [75] C. Jarlskog. A basis independent formulation of the connection between quark
885 mass matrices, CP violation and experiment. *Zeitschrift für Physik C Particles*
886 *and Fields*, 29(3):491–497, sep 1985.
- 887 [76] B J P Jones, C S Chiu, J M Conrad, C M Ignarra, T Katori, and M Toups. A
888 measurement of the absorption of liquid argon scintillation light by dissolved ni-
889 trogen at the part-per-million level. *Journal of Instrumentation*, 8(07):P07011,
890 2013.
- 891 [77] Benjamin J. P. Jones. *Sterile Neutrinos in Cold Climates*. PhD thesis, MIT,
892 2015.

- 893 [78] Cezary Juszczak, Jarosław A. Nowak, and Jan T. Sobczyk. Simulations from
894 a new neutrino event generator. *Nuclear Physics B - Proceedings Supplements*,
895 159:211–216, sep 2006.
- 896 [79] D. I. Kazakov. Beyond the standard model: In search of supersymmetry. In
897 *2000 European School of high-energy physics, Caramulo, Portugal, 20 Aug-2*
898 *Sep 2000: Proceedings*, pages 125–199, 2000.
- 899 [80] Dae-Gyu Lee, R. N. Mohapatra, M. K. Parida, and Merostar Rani. Predictions
900 for the proton lifetime in minimal nonsupersymmetric $so(10)$ models: An update.
901 *Phys. Rev. D*, 51:229–235, Jan 1995.
- 902 [81] M A Leigui de Oliveira. Expression of Interest for a Full-Scale Detector Engi-
903 neering Test and Test Beam Calibration of a Single-Phase LAr TPC. Technical
904 Report CERN-SPSC-2014-027. SPSC-EOI-011, CERN, Geneva, Oct 2014.
- 905 [82] W. H. Lippincott, K. J. Coakley, D. Gastler, A. Hime, E. Kearns, D. N. McK-
906 insey, J. A. Nikkel, and L. C. Stonehill. Scintillation time dependence and pulse
907 shape discrimination in liquid argon. *Phys. Rev. C*, 78:035801, Sep 2008.
- 908 [83] Jorge L. Lopez and Dimitri V. Nanopoulos. Flipped SU(5): Origins and re-
909 cent developments. In *15th Johns Hopkins Workshop on Current Problems*
910 *in Particle Theory: Particle Physics from Underground to Heaven Baltimore,*
911 *Maryland, August 26-28, 1991*, pages 277–297, 1991.
- 912 [84] Vincent Lucas and Stuart Raby. Nucleon decay in a realistic $so(10)$ susy gut.
913 *Phys. Rev. D*, 55:6986–7009, Jun 1997.
- 914 [85] Ettore Majorana. Teoria simmetrica dell'elettrone e del positrone. *Il Nuovo*
915 *Cimento*, 14(4):171–184, apr 1937.

- 916 [86] Hisakazu Minakata and Alexei Yu. Smirnov. Neutrino mixing and quark-lepton
917 complementarity. *Phys. Rev. D*, 70:073009, Oct 2004.
- 918 [87] M. Mooney. The microboone experiment and the impact of space charge effects.
919 2015.
- 920 [88] E. Morikawa, R. Reininger, P. Gurtler, V. Saile, and P. Laporte. Argon, kryp-
921 ton, and xenon excimer luminescence: From the dilute gas to the condensed
922 phase. *The Journal of Chemical Physics*, 91(3):1469–1477, aug 1989.
- 923 [89] FM Newcomer, S Tedja, R Van Berg, J Van der Spiegel, and HH Williams.
924 A fast, low power, amplifier-shaper-discriminator for high rate straw tracking
925 systems. *IEEE Transactions on Nuclear Science*, 40(4):630–636, 1993.
- 926 [90] Emmy Noether. Invariant variation problems. *Transport Theory and Statistical
927 Physics*, 1(3):186–207, jan 1971.
- 928 [91] I. Nutini. Study of charged particles interaction processes on ar in the 0.2 - 2.0
929 GeV energy range through combined information from ionization free charge
930 and scintillation light. Technical report, jan 2015.
- 931 [92] D. R. Nygren. The time projection chamber: A new 4π detector for charged
932 particles. Technical report, 1974.
- 933 [93] L. Onsager. Initial recombination of ions. *Phys. Rev.*, 54:554–557, Oct 1938.
- 934 [94] S. Pascoli, S.T. Petcov, and A. Riotto. Leptogenesis and low energy cp-violation
935 in neutrino physics. *Nuclear Physics B*, 774(1):1 – 52, 2007.
- 936 [95] C. Patrignani et al. Review of Particle Physics. *Chin. Phys.*, C40(10):100001,
937 2016.

- 938 [96] B. Pontecorvo. Neutrino Experiments and the Problem of Conservation of
939 Leptonic Charge. *Sov. Phys. JETP*, 26:984–988, 1968. [Zh. Eksp. Teor.
940 Fiz.53,1717(1967)].
- 941 [97] T. Yang R. Acciarri, M. Stancari. Determination of the electron lifetime in
942 lariat. Technical report, March 2016.
- 943 [98] Martti Raidal. Relation between the neutrino and quark mixing angles and
944 grand unification. *Phys. Rev. Lett.*, 93:161801, Oct 2004.
- 945 [99] Steve Ritz et al. Building for Discovery: Strategic Plan for U.S. Particle Physics
946 in the Global Context. 2014.
- 947 [100] C. Rubbia. The Liquid Argon Time Projection Chamber: A New Concept for
948 Neutrino Detectors. 1977.
- 949 [101] L.M. Saunders. Electromagnetic production of pions from nuclei. *Nucl. Phys.*,
950 *B7*: 293-310(1968).
- 951 [102] Qaisar Shafi and Zurab Tavartkiladze. Neutrino democracy, fermion mass hier-
952 archies, and proton decay from 5d su(5). *Phys. Rev. D*, 67:075007, Apr 2003.
- 953 [103] Sigma-Aldrich, P.O. Box 14508, St. Louis, MO 63178 USA.
- 954 [104] R. K. Teague and C. J. Pings. Refractive index and the lorentz–lorenz function
955 for gaseous and liquid argon, including a study of the coexistence curve near the
956 critical state. *The Journal of Chemical Physics*, 48(11):4973–4984, jun 1968.
- 957 [105] J. Thomas and D. A. Imel. Recombination of electron-ion pairs in liquid argon
958 and liquid xenon. *Phys. Rev. A*, 36:614–616, Jul 1987.
- 959 [106] D.R.O. Morrison N. Rivoire V. Flaminio, W.G. Moorhead. Compilation of
960 Cross Sections I: π^+ and π^- Induced Reactions. *CERN-HERA*, pages 83–01,
961 1983.

- 962 [107] D.R.O. Morrison N. Rivoire V. Flaminio, W.G. Moorhead. Compilation of
963 Cross Sections II: K^+ and K^- Induced Reactions. *CERN-HERA*, pages 83–02,
964 1983.
- 965 [108] Hermann Weyl. Gravitation and the electron. *Proceedings of the National
966 Academy of Sciences of the United States of America*, 15(4):323–334, 1929.
- 967 [109] Colin et al Wilkin. A comparison of pi+ and pi- total cross-sections of light
968 nuclei near the 3-3 resonance. *Nucl. Phys.*, B62:61–85, 1973.
- 969 [110] D. H. Wright and M. H. Kelsey. The Geant4 Bertini Cascade. *Nucl. Instrum.
970 Meth.*, A804:175–188, 2015.
- 971 [111] C. S. Wu, E. Ambler, R. W. Hayward, D. D. Hoppes, and R. P. Hudson.
972 Experimental test of parity conservation in beta decay. *Phys. Rev.*, 105:1413–
973 1415, Feb 1957.
- 974 [112] N Yahlali, L M P Fernandes, K Gonzlez, A N C Garcia, and A Soriano. Imaging
975 with sipms in noble-gas detectors. *Journal of Instrumentation*, 8(01):C01003,
976 2013.
- 977 [113] T. Yanagida. Horizontal symmetry and masses of neutrinos. *Progress of Theo-
978 retical Physics*, 64(3):1103–1105, sep 1980.